Powder Reuse in Electron Beam Melting Additive Manufacturing of Ti6Al4V: Particle Microstructure, Oxygen Content and Mechanical Properties

Alexander Montelione

A thesis submitted in partial fulfillment of the requirements for the degree of

Master of Science

University of Washington

2020

Reading Committee:

Dwayne Arola, Chair

Ramulu Mamidala

Navid Zobeiry

Jeffrey Lipton

Program Authorized to Offer Degree:

Department of Materials Science and Engineering

University of Washington

Abstract

Powder Reuse in Electron Beam Melting Additive Manufacturing of Ti6Al4V: Particle Microstructure, Oxygen Content and Mechanical Properties

Alexander Montelione

Chair of the Supervisory Committee:
Professor Dwayne Arola
Department of Materials Science and Engineering

Metal Additive Manufacturing (AM) is being adopted in the aerospace and orthopedic industries. While the cost of powder feedstock has raised interest in reusing unmelted powder in subsequent builds, powder reuse could degrade part properties. In this study the properties of Ti6Al4V metal powder are evaluated over 30 build cycles in Electron Beam Melting (EBM) AM. The morphological, microstructural, mechanical, and chemical changes are evaluated in cross-sectioned powder particles and compared to control samples. Results show that in response to the elevated build chamber temperature, the powder undergoes a sub-beta-transus aging heat treatment with reuse. Nanoindentation shows that the particles undergo an increase in near-surface hardness (up to 2 GPa) with respect to the core. Tint etching revealed an oxidized surface layers consistent with alpha case formation. The particle hardening appears to result from oxygen diffusion during powder recovery and not work hardening via mechanical aspects of powder recovery.

TABLE OF CONTENTS

LIST OF FIGURES

LIST OF TABLES

ACKNOWLEDGEMENTS

First and foremost, I would like to thank Professors Dwayne Arola and Ramulu Mamidala for their continued support and encouragement of my pursuit of the Master of Science. Additionally, I would like to thank Professors Jeffrey Lipton and Navid Zobeiry for being a part of my defense committee. I also want to thank Micah Glaz, Tatyana Galenko, Dan Graham, and Bill Kuykendall for their training and instruction on the equipment that made this thesis possible. Finally, I would like to thank my friends and family, as without their support none of this would be possible.

DEDICATION

This work is dedicated to Ellie, who keeps me most accountable

Chapter 1. OVERVIEW

The primary objective of this investigation is to evaluate the changes in properties of titanium powder with its reuse in EBM AM. The effort explores oxygen contamination of the powder with reuse over a large number of build cycles, and the primary contributing mechanisms, through a quantification of changes in the microstructure and mechanical properties of individual powder particles. Results of the various methods of quantification are discussed in detail and the implication to future powder reuse strategies are discussed.

1.1 METAL ADDITIVE MANUFACTURING

Additive Manufacturing (AM) refers to the process of developing a complex three-dimensional shape progressively through the addition of new material according to a digital model. It is defined by ISO/ASTM terminology to be the "process of joining materials to make parts from 3D model data, usually layer upon layer, as opposed to subtractive manufacturing and formative manufacturing methodologies."[1] In this process, a three-dimensional model of the final component is digitally sliced into two-dimensional cross-sections. These cross-section blueprints are fed to a machine which generates a tool path to form the layers by selectively joining the base material, typically in the form of wire, powder, or sheets. The result is a faithful recreation of the modeled part. Since AM is not restricted to conventional shaping processes or commercial material shapes, much more design freedom is allowed in the modeling of the components [2]. For example, internal cooling channels that could not be created by machining can be easily introduced to parts made by AM. Another significant advantage of AM comes with part reduction in assemblies. Where previously complex assemblies were created by the joining of multiple sub-components,

now manifolds and fuel injectors can be built entirely in a single step, saving time and assembly cost. By allowing increasing complexity in part design without increasing production cost, AM provides a powerful tool for building highly optimized structures at an economic cost.

AM technologies are broadly classified into seven categories: vat photopolymerisation, material jetting, binder jetting, material extrusion, powder bed fusion, sheet lamination, and directed energy deposition. This work focuses exclusively on the powder bed fusion process.

Powder Bed Fusion (PBF) is a category of additive manufacturing processes in which thermal energy selectively fuses regions of a powder bed to create the two dimensional cross-sections used to build the three-dimensional part [1]. The feedstock of this process is typically a polymer or metal alloy powder, which is fused solid by a heat source, often in the form of a laser or electron beam. Metal PBF AM processes have become increasingly viable for applications in the aerospace and medical industries [2, 3].

1.2 Electron Beam Melting Additive Manufacturing

Electron Beam Melting (EBM) is one of the most prominent methods for metal PBF AM. Similar to other PBF methods, this process uses an electron beam as the heat source to selectively melt and fuse metal powder layer-by-layer in the process of achieving the desired 3D geometry [4]. However, EBM AM is distinct from other PBF in a few key areas. The most notable distinctions are the fact that the entire build chamber is kept under high vacuum during the build process, and that the powder bed is heated to the point where the powder particles just begin to sinter together. The sintering results in a solid – if weak – block of powder, which supports the parts being printed. This reduces the need for extensive support structures that are characteristic of deposition processes [4]. However, the powder bed volume increases the quantity of powder feedstock needed to complete the build process, regardless of the part volume. Only a fraction of the powder in the

build chamber is melted and utilized in the part. The remaining/surrounding powder is available for reuse after completion of the build and its recovery.

As a consequence of the relatively high cost of feedstock material, powder reuse is now considered an essential part of the PBF process and critical to maximizing the affordability of the process [5-7]. Indeed, a number of studies have been reported on various aspects of metal powder reuse in AM. Overall, prior investigations on reuse have distinguished that the powder quality can undergo changes with reuse that manifest through degradation in the mechanical properties of the metal [6-9]. Thus, powder reuse poses an important trade-off between process economics and part performance concerns.

1.3 Oxidation of Titanium

Due to a combination of their excellent strength to weight ratios, biocompatibility and corrosion resistance, titanium alloys are used extensively in aerospace and medical applications[2, 10, 11]. Titanium alloys are also a major focus for studies investigating metal AM via EBM [11-13] and Selective Laser Melting (SLM) [11, 12, 14]. The chemical resistance of titanium comes from its reactivity with oxygen. It forms an impervious surface oxide layer spontaneously in the presence of oxygen that prevents the underlying metal from reacting with the surrounding environment [15]. At high temperatures, however, the oxygen can diffuse into the metal to form an interstitially hardened layer known as alpha-case (α-case) [16, 17]. The near-surface case layer is harder than the underlying metal. It is also more brittle, and often undergoes micro-cracking, which can degrade the corrosion and fatigue resistance of the metal [16]. An increase in oxidation of the powder may foster an increase in oxygen content of the printed metal and contribute to the degradation of the mechanical properties seen in components built with reused powder, as has been seen in many studies [5-9, 18, 19] This raises a concern in AM processes involving titanium and

other anodic alloys that have tendency to react with oxygen. Indeed, PBF systems for metal AM are operated in inert environments, either under argon atmosphere for SLM or under vacuum for EBM systems, in order to protect the molten metal from oxygen.

The oxygen content of titanium powder in AM processes reportedly increases with its reuse [6, 7, 18], and can exceed the allowable concentration limits outlined by material specifications. One approach to temper the rise in oxygen content is to simply mix the reused powder with virgin (unused) powder after each build cycle. While plausible, the rise in oxygen content can be both process and machine dependent, which complicates the determination of processing methods for the most efficient use of powder. It is a solution without fundamental understanding. Furthermore, there are important scientific issues related to the powder reuse beyond its exposure to elevated temperature, including the changes in particle microstructure, depth of oxidized layer, changes in mechanical properties, etc. To the authors' knowledge, a detailed investigation of powder degradation in metal PBF AM by EBM that addresses these concerns has not been reported.

1.4 Alpha Case and Ammonium Bifluoride

Alpha case (α-case) is a hardened, brittle surface case layer on titanium, often found on castings, due to the a change in surface chemistry during processing [16, 17, 20-23]. It is generally the result of oxygen diffusion into the metal at high temperature, although substitutional metallic elements can also cause an α-case layer to form[24, 25]. Oxygen stabilized α-case forms due to the high affinity of titanium for the element, which diffuses interstitially and acts as an alpha phase stabilizer and solid solution strengthener [20, 26]. The stabilizing effect of oxygen on the alpha titanium phase arises due to the higher solubility of oxygen in the alpha phase (14.5 wt%) as compared to the beta phase (1.8-3.6 wt%) [17, 20]. At around 0.2-0.3 wt.% oxygen, the titanium

undergoes a transition which leads to an increase in strength and a remarkable decrease in ductility [27-29]. It is understood that the strengthening potential of oxygen in titanium alloys comes from an interaction between the oxygen interstitial atoms and screw dislocation cores [26]. Oxygen atoms occupy the interstitial sites in the HCP lattice, thereby causing a slight tetragonal lattice distortion that stabilizes the alpha phase and impedes dislocation motion through the lattice [17, 30]. This brittle surface layer is problematic due to its lower ductility and tendency to develop microcracks, which can significantly reduce fatigue life [16, 20, 22, 26]. Due to the criticality of removing of removing this α-case layer for aerospace components, various methods have been developed to detect α-case layers in titanium. One such method is a tint etch with ammonium bifluoride, which highlights the α-case layer via a chemical process [29]. Hardness testing methods have also been developed and employed in a number of studies [16, 17, 20-22, 24] to characterize α-case depth through hardness profiles of sectioned parts.

Chapter 2. METHODS

2.1 MATERIAL

Fifty (50) kg of Grade 5 Titanium Alloy (Ti6Al4V) powder was purchased from the machine manufacturer (ARCAM: Batch P1303, Part #430944) for this study. The powder was used in sequential standardized builds performed using a commercial EBM powder bed fusion system (ARCAM, Model A2X, Sweden). A total of thirty consecutive builds were performed, with the excess powder from each build being collected and reused in the subsequent build. A standardized build was performed in each cycle, which consisted of approximately 40 cm^3 of metal, including 0.6 cm^3 of support metal. The total volume of metal powder in the build chamber was 2966 cm^3, based on a total build height of 104 mm. The build chamber was preheated to 650°C for each build,

according to the default machine theme. The average build time for each cycle was approximately 16 hours, giving a total build time of approximately 480 hours for all 30 builds. More details are listed in Ghods et al. [31]. After each build, the partially sintered powder block was removed from the ARCAM machine and transferred to the powder recovery system (PRS). There, compressed air and loose titanium powder was used to free the encapsulated printed parts from the sintered powder block and loosen the remaining powder. This volume of processed powder was mixed with the powder remaining in the hoppers of the EBM machine, sieved (#125 mesh) to remove large particles, and returned to the machine for the next build cycle.

2.2 Sample Collection

2.2.1 *Reused Powder*

Small volumes (approx. 30g) of powder were collected prior to each build cycle. These samples were identified as b1-b30, with the number corresponding to the build cycle in which the powder was used; the b1 powder sample represented powder used in the 1st build, and the b30 powder sample represented powder used in the 30th build, for example. The number therefore indicates the level of reuse of the powder, with b1 powder being in the as-received (virgin) condition, and b30 being the most reused, having underwent 29 previous cycles.

2.2.2 *Accelerated PRS Powder*

A separate batch of virgin powder was run continuously through the PRS system for 30 hours to simulate the effects of the repeated air blasting on an accelerated schedule. This powder underwent the mechanical deformation associated with the recovery process without the effects of the thermal variations associated with the build cycles. Samples of this powder were taken after every 10 hours of PRS treatment for analysis, and labeled t10, t20 and t30.

2.2.3 *Alpha Case Standard*

To validate the methods used to detect the presence of an alpha case in the samples, a lab standard was produced using available materials. A sample of virgin powder was subjected to a furnace heat treatment at 760°C for 2 hours in ambient air, followed by air cooling. The conditions were selected based on a previous study reported by Pitt and Ramulu[32] investigating alpha case development on titanium.

2.3 SAMPLE PREPARATION

The powder samples were first mounted in Struers EpoFix two-part epoxy resin within a square plastic mold (approx. 1 cm x 1 cm) to establish a shape that helped to index and track individual powder particles. To aid in the impregnation of the powder samples with epoxy, they were placed in a vacuum chamber after adding the epoxy to the mold. After setting, the square powder mount samples were extracted from the plastic mold and then mounted in 30 mm cylindrical molds involving the aforementioned epoxy resin. Once cured, the powder samples were ground using silicon carbide papers with successively smaller particles to #800 grit. Polishing was then performed using 6 and 3 μm DiaLube diamond particle suspensions on an Allied High Tech White Label pad and a Struers MD-Dac pad, respectively. The final polish was achieved using a 0.05 μm colloidal silica attack polish solution containing 5% ammonium hydroxide and a small amount of hydrogen peroxide, on a Struers MD-Chem pad.

2.4 SAMPLE ANALYSIS

2.4.1 *Optical Microscopy*

The polished samples were etched, starting with Kroll's reagent (etchant #192 of ASTM E407-07[33]) by partial immersion for 10 seconds, followed by an ammonium biflouride (ABF) tint etch

(etchant #217 of ASTM E407-07 [33]). Figure 2.1 shows an alpha case layer revealed by this tint etching process on a wrought bar of Ti6Al4V; the alpha case layer appears bright relative to the remainder.

The powder samples were evaluated using an Olympus BX51M reflected light microscope equipped with 5x, 10x, 20x, 50x, and 100x objective lenses. The samples were evaluated in the as-polished, etched, and tinted conditions to monitor changes resulting from the recycling process. Particles showing interesting features were indexed using a simple coordinate system for later evaluation by nanoindentation and SEM-EDS.

After optical analysis, the samples were repolished using the aforementioned methods to remove the etched topography and re-establish a smooth surface with mirror finish, as required for nanoindentation and SEM analysis.

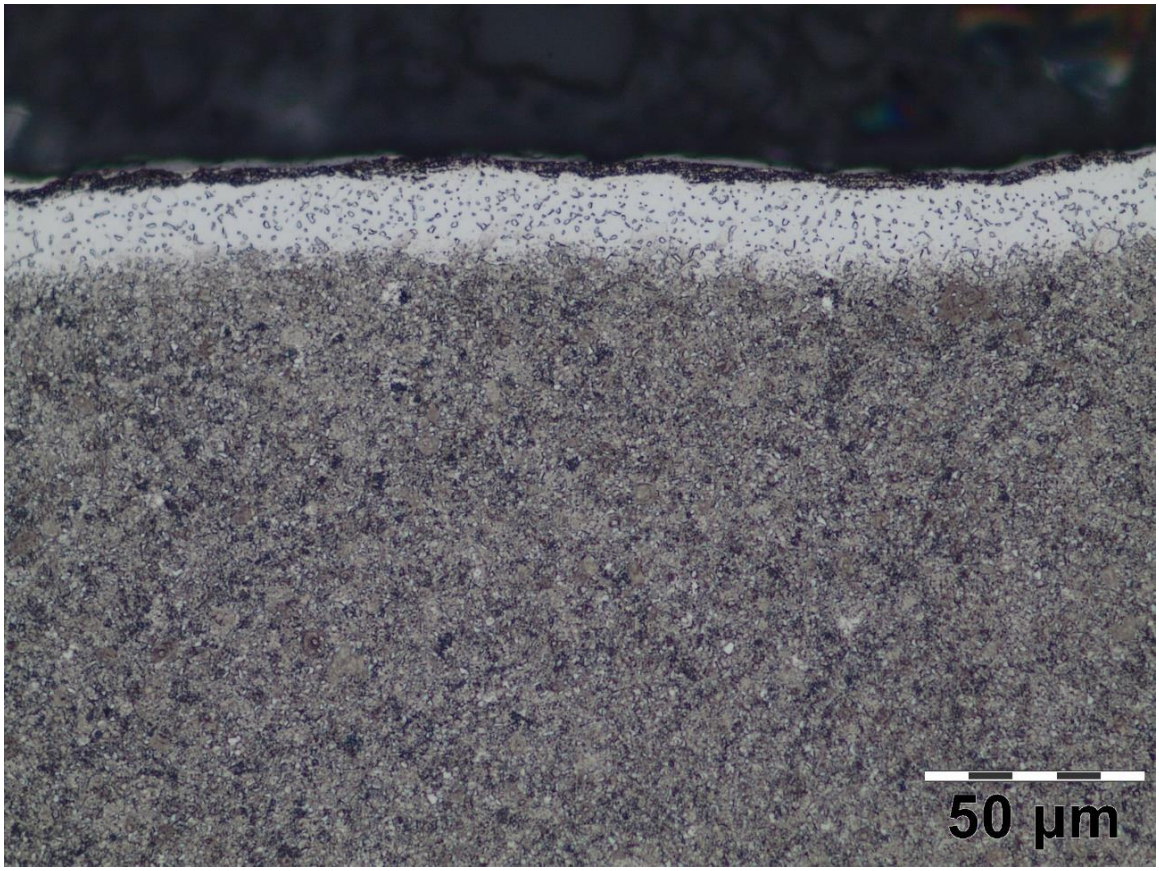

Figure 2.1. Wrought Ti6Al4V etched with Kroll's and ABF, showing a white alpha-case layer.

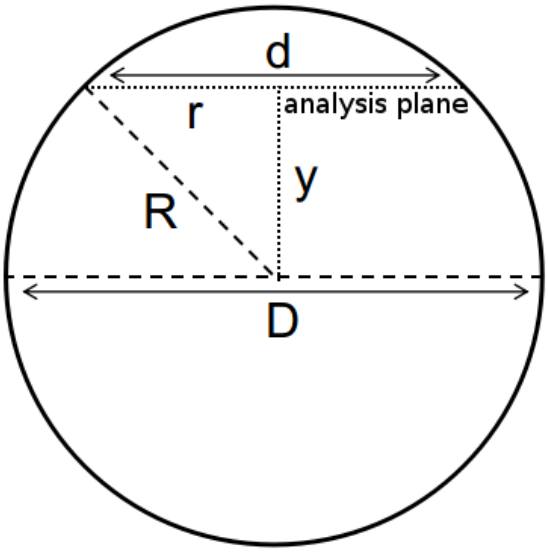

Figure 2.2. Schematic diagram of dimensions used in calculating the true void diameter from the measured cross-section.

2.4.2 *Void Analysis by Optical Microscopy*

Void size and concentration in the powder was measured in the as-polished condition using image analysis software. For void size, 500x magnification images were taken of the voids and their caliper diameters were measured in 8 directions and averaged. Void concentration was measured on random fields of view throughout the sample. 100x magnification images were taken and analyzed using a custom ImageJ script to count the number of particles and voids in each image.

It is important to note that the voids were measured on a random cross-sectional plane, and their actual diameter in the particle cannot be directly measured. However, if the voids are assumed to be spherical and are intersecting the evaluation plane at random points, the true size of the voids can be calculated based on the predicted area of the cross-section. Since it is equally probable to intersect the void at any point, the expected cross-sectional area becomes the average cross-sectional area as a function of height. For a spherical void sectioned randomly as depicted schematically in Figure 2.2. Schematic diagram of dimensions used in calculating the true void diameter from the measured cross-section.Figure 2.2, the pore dimensions are described by equation 2.1 where $\bar{a}$ is the average cross-sectional area, R is the true particle radius, and y is the distance of the intersecting plane from the center of the pore. The average cross-sectional area can be related to the measured radius r and the true radius R according to equation 2.2. Then, the final relation between r and R, which is the same as the relation between the measured diameter d and the true diameter D is given by equation 2.3.

$$\bar{a} = \frac{1}{R-(-R)} \int_{-R}^{R} \pi(R^2 - y^2)\, dy \tag{2.1}$$

$$\bar{a} = \sqrt{\frac{2}{3}}\pi R^2 = \pi r^2 \tag{2.2}$$

$$\mathrm{R} = \sqrt{\frac{3}{2}} r \rightarrow D = \sqrt{\frac{3}{2}} d \tag{2.3}$$

2.4.3 *Nanoindentation*

Hardness measurements were made on the cross-sectioned powder particles using a commercial nanoindenter system (Bruker Hysitron TriboIndenter 980, USA) with a Berkovich diamond indenter and tip radius of approximately 190 μm. A 2 mN indentation load was chosen such that the indents produced were small enough to be placed within a few microns from the edge of the particle, while deep enough to avoid complications from surface topography, contamination and indenter tip geometry. Under a 2 mN load, the indents had an edge length of approximately 1 μm and were approximately 100 nm deep. Examples of typical indents obtained are shown in Figure 2.3. The testing conditions enabled indents to be placed as close as 2.5 μm from the edge of the particle, while abiding by the indent spacing requirements outlined in ASTM E 384-17 [34].

The powder sample mounts were secured to the nanoindenter stage using vacuum suction. For each particle investigated within a mount, a profilometer scan was taken and the desired indent locations were specified manually. The indent locations were chosen to obtain at least 3 indents close to the surface, a staggered array progressing inward to the core, and 5 indents near the center of the particle. The indents were examined using scanning probe microscopy to ensure that the indents were placed in the desired locations. These scans were also used to measure the radial distance from the indent center to the nearest edge.

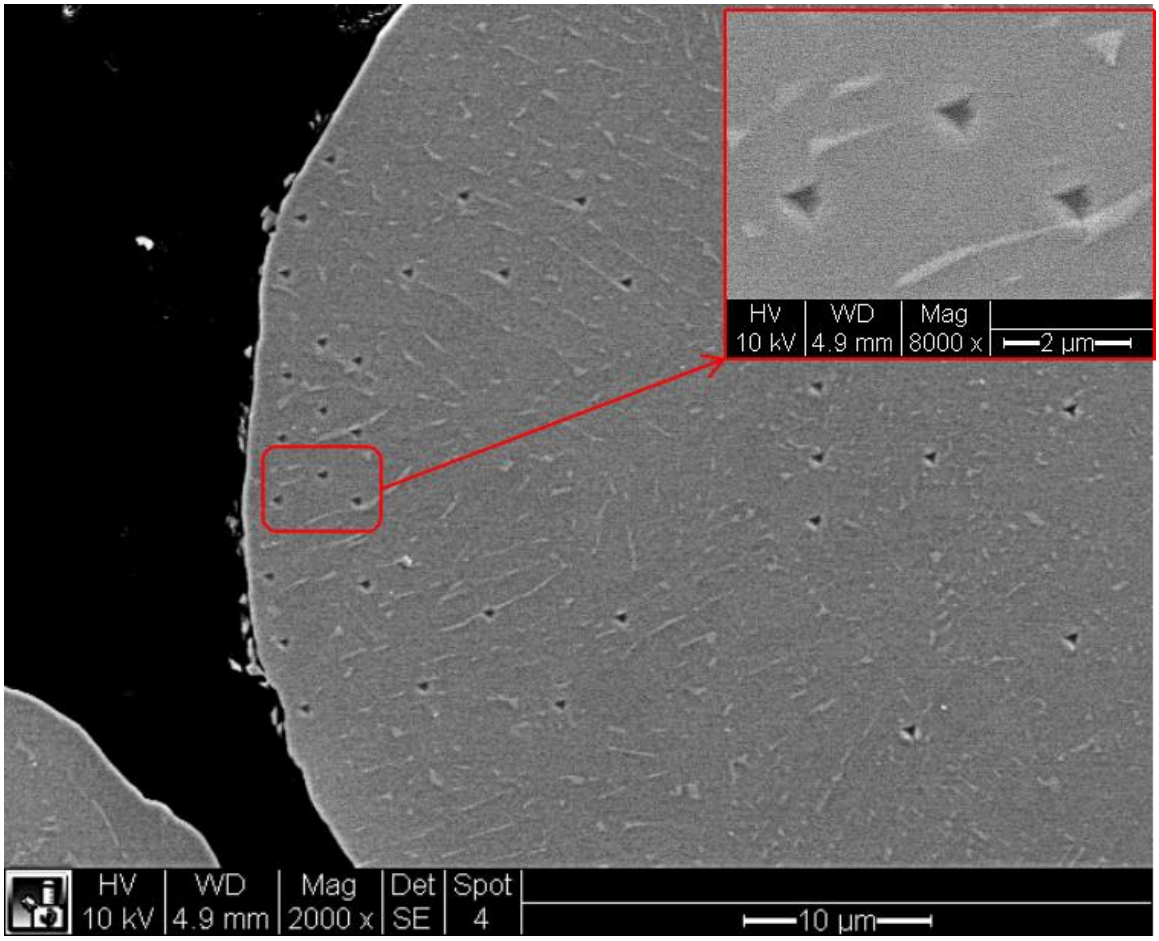

Figure 2.3. SEM micrograph of b30p19 after nanoindentation testing. Indents are visible on the surface. Inset shows detail of the indents.

The hardness and elastic modulus of the particles were evaluated using the standard approach detailed by Oliver and Pharr [35]. A representative load-displacement curve taken from a particle without significant surface hardening is shown in Figure 2.4, along with a schematic of a typical nanoindentation load-displacement curve, with quantities marked. The load-displacement curves were analyzed by the machine software using equations 2.4 and 2.5 below to determine the reduced modulus (E_r) and the hardness (H).

$$S = \frac{dP}{dh} = \frac{2}{\sqrt{\pi}} E_r \sqrt{A} \tag{2.4}$$

$$H = \frac{P_{max}}{A} \tag{2.5}$$

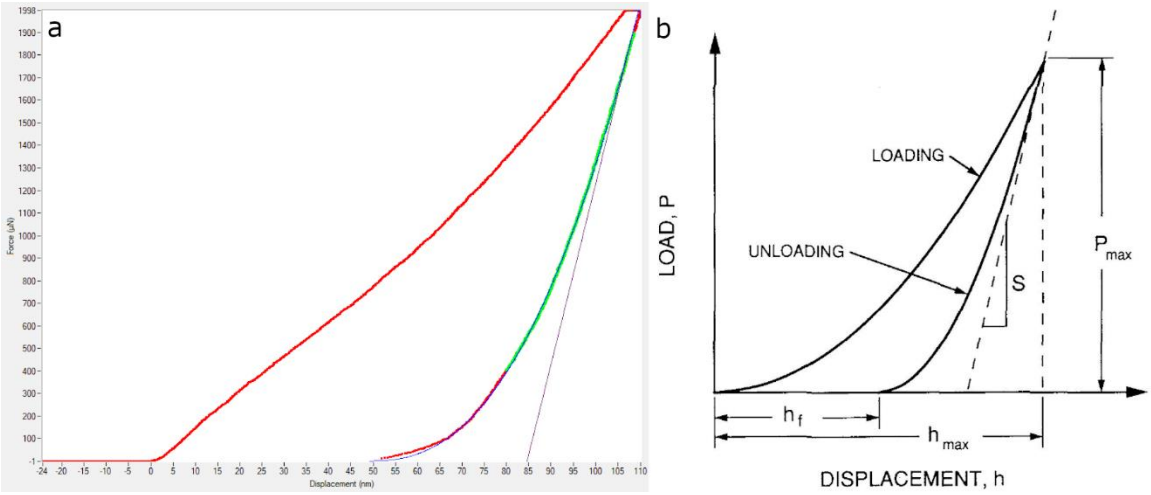

Figure 2.4. (a) representative nanoindentation load-displacement curve for low oxygen particles, and (b) schematic showing a typical nanoindentation load-displacement curve. The indicated values are the peak indentation load (P_{max}), the indenter displacement at peak load (h_{max}), the final depth of the contact impression after unloading (h_f), and the initial unloading stiffness (S).

Where S is the unloading stiffness, calculated from the initial slope of the load (P) and displacement (h) curve upon unloading. A represents the projected area of the elastic contact, derived from the geometry of the tip and the displacement. The elasticity of the indenter tip contributes to E_r by the relation in equation 2.6, where E and v are the Young's Modulus and Poisson's ratio for the specimen, and E_i and v_i are the same parameters for the indenter.

$$\frac{1}{E_r} = \frac{(1-v^2)}{E} + \frac{(1-v_i^2)}{E_i} \tag{2.6}$$

The nanoindentation hardness measurements were used to evaluate the presence of an alpha case layer and the potential for work hardening of the particles resulting from the PRS process. A hardness differential of 0.4 GPa between the surface and the core was used as the criteria for defining alpha case, which is based off an AMS material specification that defines surface contamination by a surface hardness more than 40 points higher than the subsurface hardness on the Knoop scale using a 200-gram load [36]. This requirement was adapted to nanoindentation methods to define alpha case. Defining the limit by hardness meant that the reduced modulus was largely disregarded for this evaluation.

The size of the indents needed to obtain reliable readings of the hardness effectively limited how close they could be placed to the surface. Indents within 2.5 μm of the edge were considered invalid by the spacing requirements of ASTM E 384-17 [34]. Similarly, those with inconsistent shape and indents placed on surface irregularities were discarded as well. Consequently, indents between 2.5 μm and 5 μm of the surface were considered representative of the surface hardness. The core hardness was defined as the average of 5 indents placed roughly in the center of the particle.

2.4.4 *SEM/EDS*

An elemental analysis of the particles was performed using a commercial Scanning Electron Microscope (SEM; Phillips, Model XL30 Sirion FEI) equipped with an Energy-Dispersive x-ray Spectroscopy (EDS) detection system. The samples were carbon-coated prior to analysis to improve surface conductivity and prevent artifacts from sample charging. The EDS spectra were obtained with an accelerating voltage of 15 kV and a working distance of 5 mm. The beam spot size was adjusted to achieve a detector dead time of 30-50% for optimal signal collection. Surface-to-core line scans were taken to measure compositional gradients in the particles. The intensity of the oxygen signal was recorded as a function of distance from the particle edge.

2.4.5 *ToF-SIMS*

Data was collected on an IONTOF TOF.SIMS 5 spectrometer using Bi^{3+} ions. Images and spectra were acquired over a 125×125 micron area at 256×256 pixels. For High Mass Resolution (HMR) data, the primary ion current was 0.25 pA and signal was acquired to total dose of 9.8×10^{11} ions/cm^2. For Delayed Extraction (DE) data, the primary ion current was 0.05 pA and data was acquired to total dose of 9.9×10^{11} ions/cm^2.

An argon pre-sputter step was used to remove the passive surface oxide layer that develops spontaneously on the polished surface when exposed to air. The argon beam primary current was 7.3 nA at an accelerating voltage of 20kV. An area of 500×500 microns centered on the acquisition location was exposed to a total dose of 4.4×10^{15} ions/cm^2 over the course of 4 minutes. Analysis spectra were taken after 2 minutes of sputtering and again after 4 minutes, with the 4-minute analysis being the focus of the report.

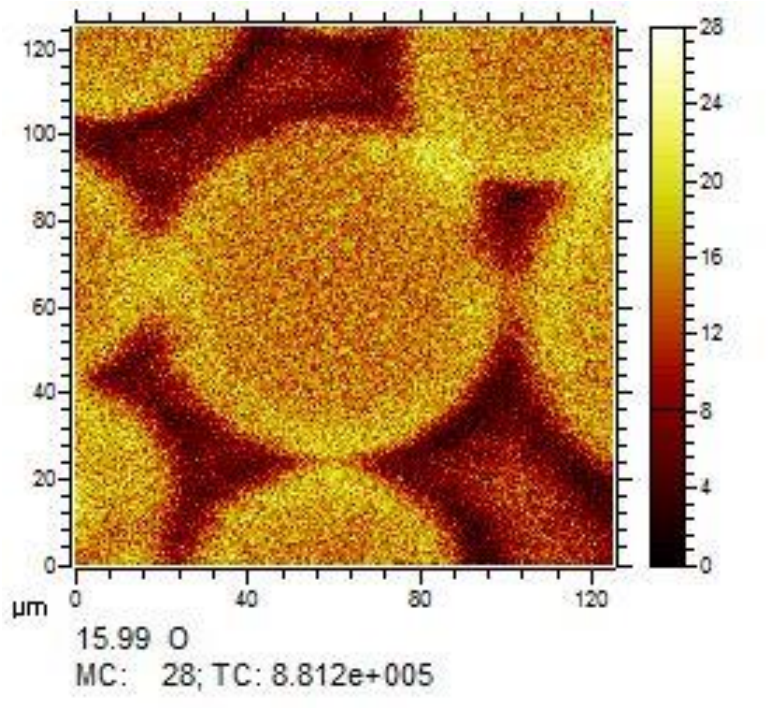

Figure 2.5. Typical intensity heat map obtained from ToF-SIMS analysis. Bright areas are areas of higher signal intensity, indicating higher concentration of that element.

2D intensity heat maps were obtained for selected ion channels. An example of one of these heat maps is shown in Figure 2.5. The heat maps were imported into ImageJ analysis software and the intensity profiles were extracted using the Radial Profile Extended plugin [37]. The plugin produces a profile plot of normalized integrated intensities as a function of radial distance from a defined point in the image, where the intensity at any given radial distance represents the sum of the pixel values around a circle of that radius. The integrated intensity is divided by the number of pixels in the circle, yielding normalized comparable values[37]. This allowed for quick, qualitative assessment of how the signal intensity changed across the particle cross-section.

Chapter 3. RESULTS

3.1 OPTICAL MICROSCOPY

3.1.1 *Virgin Powder*

A photomicrograph showing the structure of the virgin powder particles is shown in Figure 3.1. The sample b1 (virgin) powder showed a microstructure consisting entirely of martensitic alpha prime (α'). This structure consists of fine, nearly indistinguishable acicular grains of alpha phase, and forms upon fast cooling from the beta phase. Tint etching with ABF highlighted the acicular structure but revealed no alpha case layer on the particles. The particles were spherical, with small satellite particles occasionally visible along the margins of larger particles.

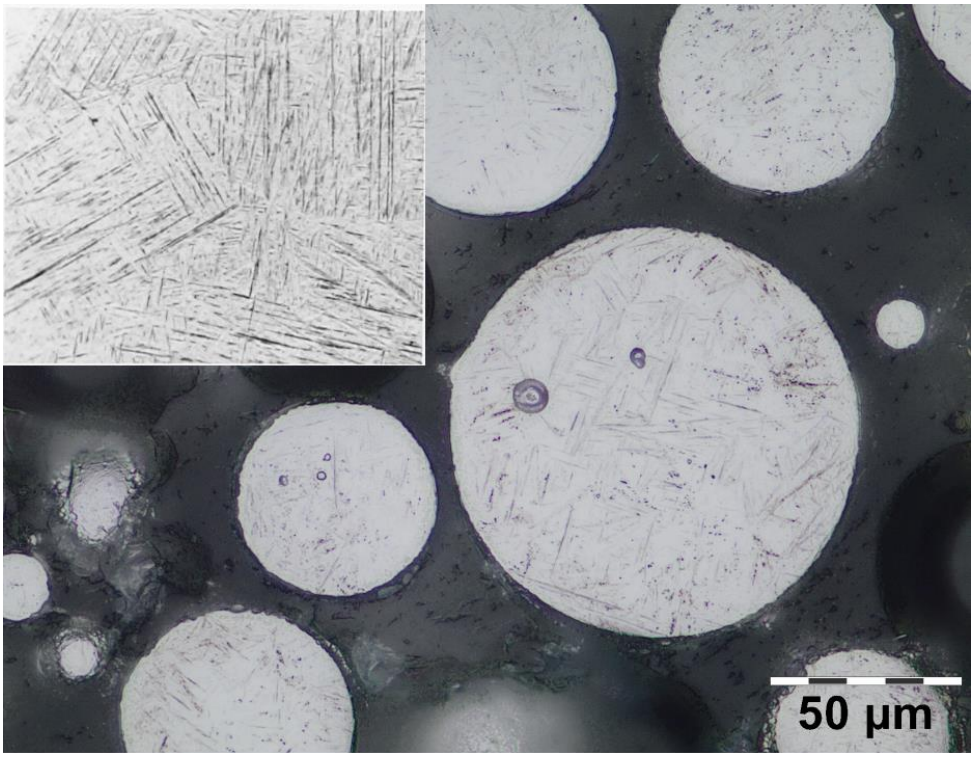

Figure 3.1. Optical micrograph showing typical microstructure of b1 powder in the etched condition. Insert shows Figure 2727 of ASM Metals Handbook Vol. 7, 8th Ed. showing a microstructure consisting entirely of alpha prime (martensite) formed in Ti-6Al-4V forged at 1900 F, air cooled, annealed for 2 hours at 1300 F and quenched in water (Kroll's etch) [38]

3.1.2 *Reused Powder*

A photomicrograph showing the structure of the reused powder particles of b30 is shown in Figure 3.2. The reused powder showed a distribution of microstructures, ranging from near-virgin martensitic alpha to heavily coarsened alpha platelets with intergranular beta. Intermediate structures were visible in individual particles showing progressive levels of coarsening of the alpha grains, suggesting that individual powder particles experienced significantly different thermal histories. A view of the changes in microstructure over the reuse program is shown in Figure 3.3. Specifically, a selection of particles from b7 and b14 are shown in Figure 3.3(a-c) and (b-f), with the coarsest microstructure from b14 shown in Figure 3.3(f). The extent of

observed coarsening and the range of the distribution of microstructures both increased with increasing reuse cycles. Specifically, the nearly virgin powder used in the early builds exhibited a few coarsened particles, whereas the powder in the later builds consisted almost entirely of heat-affected particles with relatively few particles still showing the virgin microstructure.

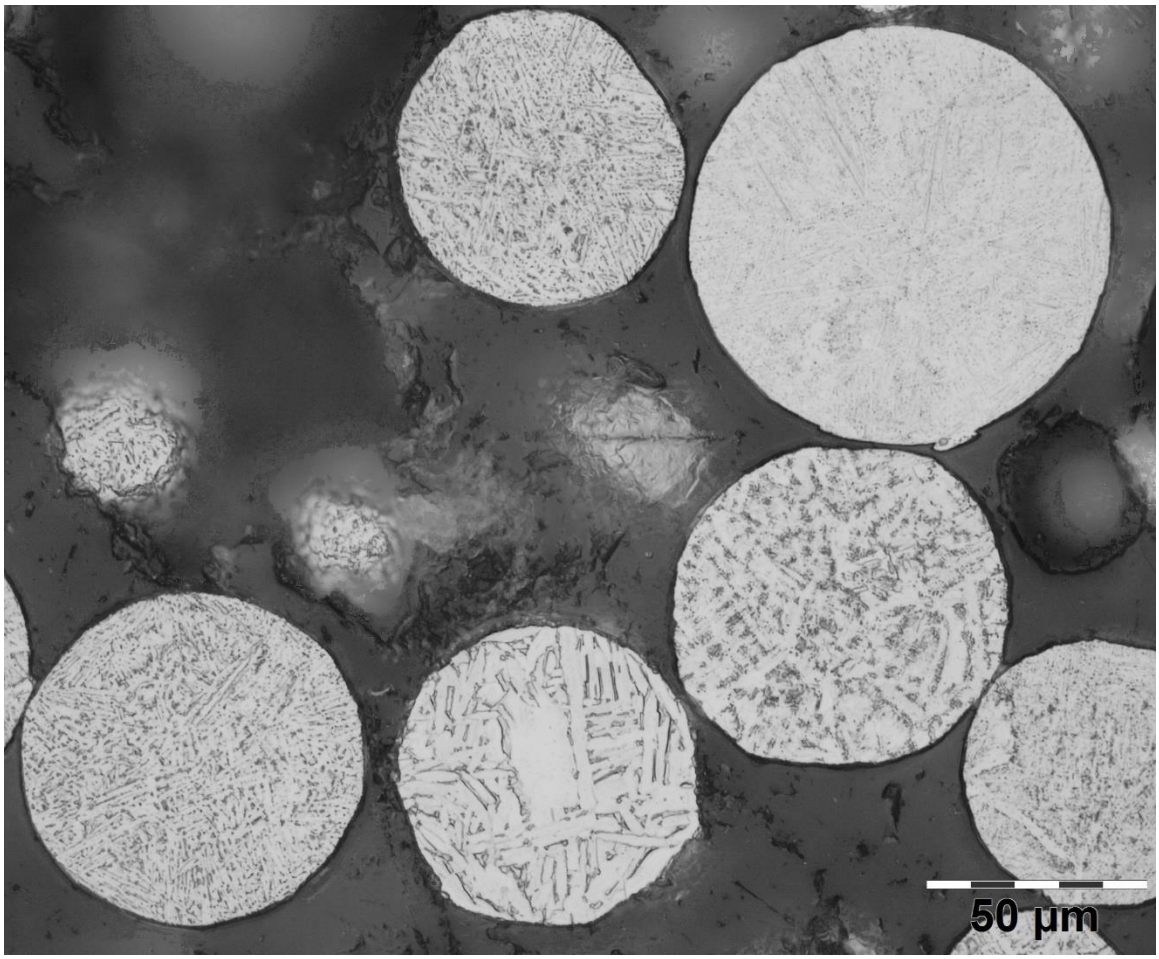

Figure 3.2. Optical micrograph of b30 powder in the etched condition, showing a range of the typical microstructures observed. The upper right particle shows a structure similar to the virgin powder, and the bottom-middle particle shows a heavily coarsened structure.

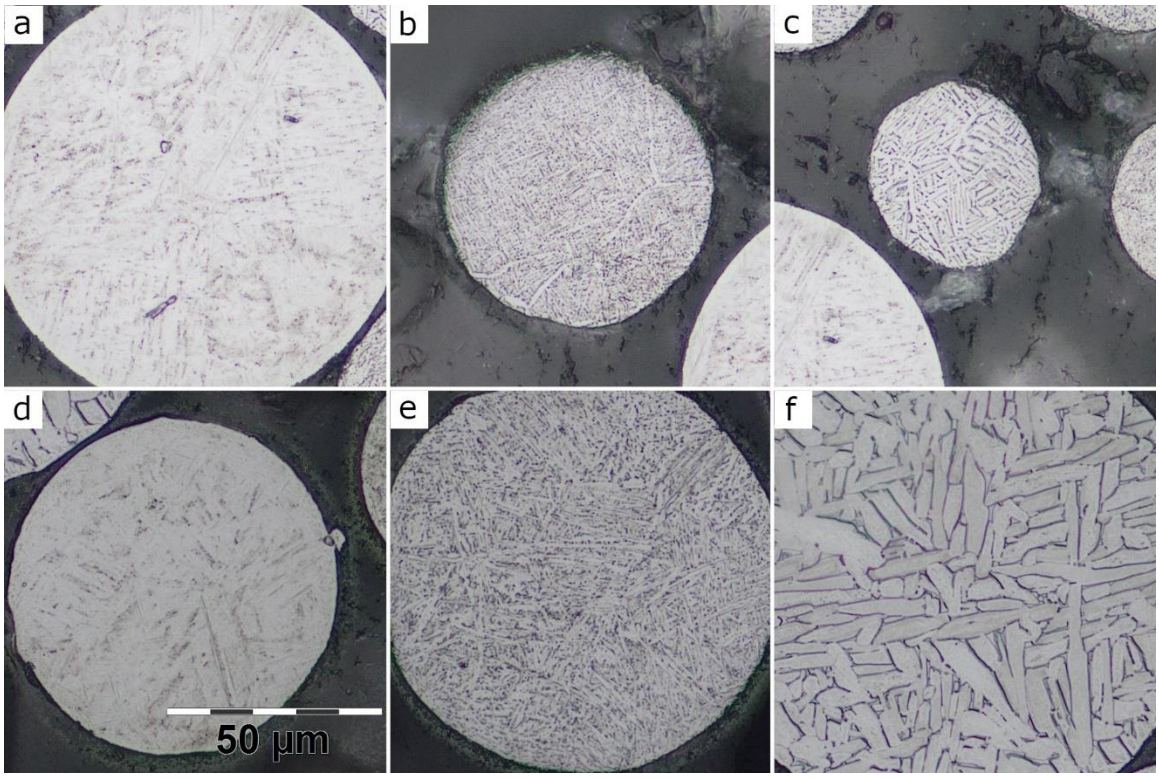

Figure 3.3. Optical micrographs from (a-c) b7 powder and (d-f) b14 powder showing ranges of observed microstructures; Kroll's etch.

3.1.3 *Alpha Case Standard*

Photomicrographs of the heat-treated powder (sample a1) under various etch conditions are shown in Figure 3.4. Cross-sectioned particles are shown in the as-polished condition in Figure 3.4(a), after being etched with Kroll's reagent in Figure 3.4(b), and after etched with Kroll's and ABF in Figure 3.4(c). Note the oxide layer surrounding each particle evident from the bright circumferential ring. The heat-treated powder showed significant deterioration as a result of the thermal oxidation. When removed from the furnace the powder was a matte orange-brown, visibly indicating the presence of a titanium oxide layer. In cross-section, a gray titanium oxide layer was visible on all the particles, coating them to a depth of approximately 10 µm. Surface cracks, chips, and crevasses were evident on the surfaces of the particles in the as-polished state as evident in all views in Figure 3.4. The microstructure of the particles consisted of acicular alpha (transformed

beta) that was not significantly coarsened from the martensitic virgin structure, owing to the relatively short duration of the heat treatment. The ABF tint etch revealed a thick white-etching, approximately 25 μm thick. Accurate total depth measurements of the white layer could not be measured from the cross-section, owing to the spherical geometry of the particles.

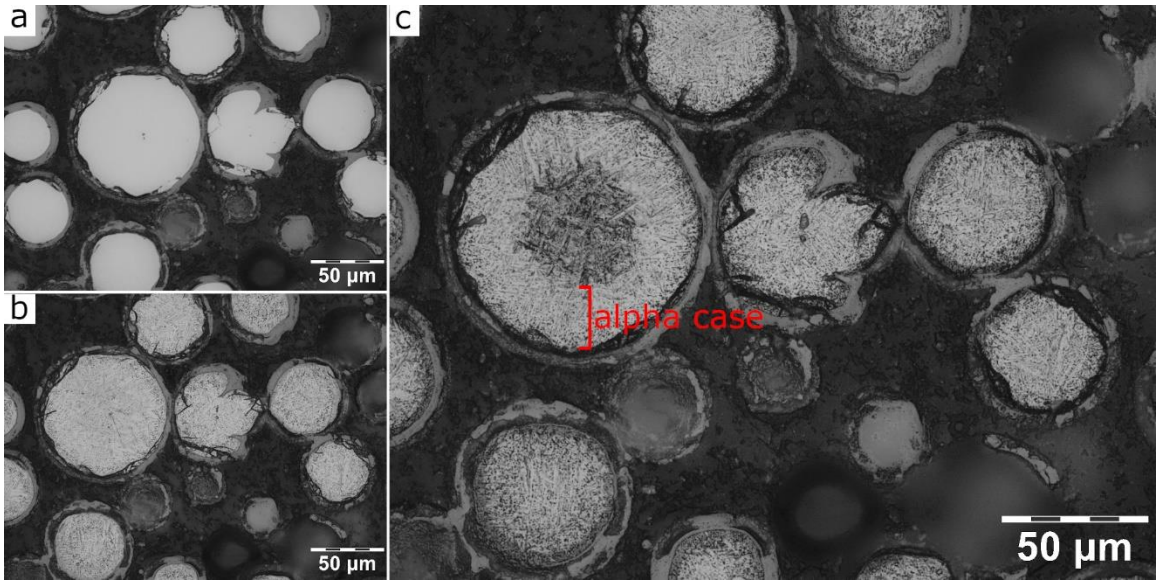

Figure 3.4. Optical micrographs from a1 powder showing particles in (a) as-polished, (b) Kroll's etch, and (c) Kroll's and ABF etch conditions. The extent of the alpha case is indicated on the particle in (c)

3.1.4 *Accelerated PRS Powder*

Photomicrographs of the particles subjected to the accelerated PRS treatment and after being etched with Kroll's and ABF are shown in Figure 3.5. Many of the particles showed flattened faces and irregular, angular morphologies, a result of deformation caused by the impact forces experienced during the PRS treatment. In some instances, particles with large internal voids were observed to have fractured from the stress of the impacts, such as that shown in Figure 3.6. The majority of the particles exhibited a fine martensitic structure when etched, similar to the microstructure of the virgin powder. A small percentage of the particles in the powder sample that

underwent 30 hours of PRS cycling (t30) demonstrated coarsened microstructures and white etching layers when etched. These observations were attributed to errant particles trapped in the system from previous build and recovery cycles, and the particles showing these features were omitted in further analysis.

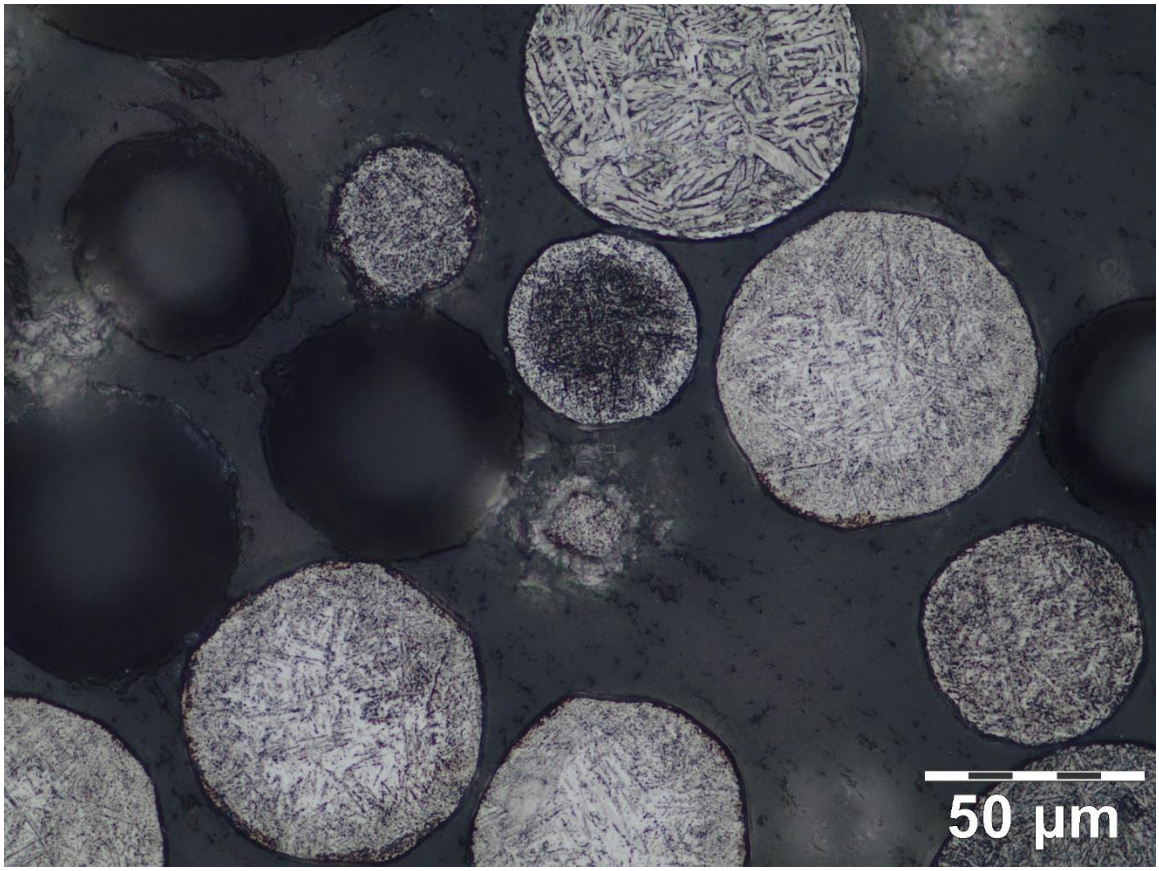

Figure 3.5. Representative photomicrograph showing particles from the t30 powder sample (accelerated PRS powder) etched with Kroll's and ABF. Note the coarser microstructure on some of the particles, as well as the visible white layer on the center particle, suggesting these particles have experienced thermal cycling.

3.1.5 *Voids*

Voids were observed in all powder samples, and ranged in size from nearly indistinguishable to encompassing the entire particle volume. Examples of large voids observed in selected particles are shown in Figure 3.6. The voids were consistent in shape, primarily round or oblong, except for the cases where the void encompassed the majority of the particle volume, resulting in structural instability and deformation.

The distribution in average measured void diameters is shown for selected powder samples over the powder reuse program in Figure 3.7(a). No significant trend was observed in the void size as a function of build number for the reused powder. Image analysis measurements of the voids documented in the particles gave an overall average measured void diameter of 29±12 μm, and a calculated true diameter of 35±15 μm. The distribution in void occurrence is plotted for selected builds of the reused powder in Figure 3.7(b). The frequency of void occurrence in the powder was determined to be about 1 void for every 100 particles, or a 1% void occurrence. This value was consistent across all powder samples. The average measured void diameters and calculated true void diameters for selected powder samples are tabulated in Table 3.1, and the void occurrence in Table 3.2.

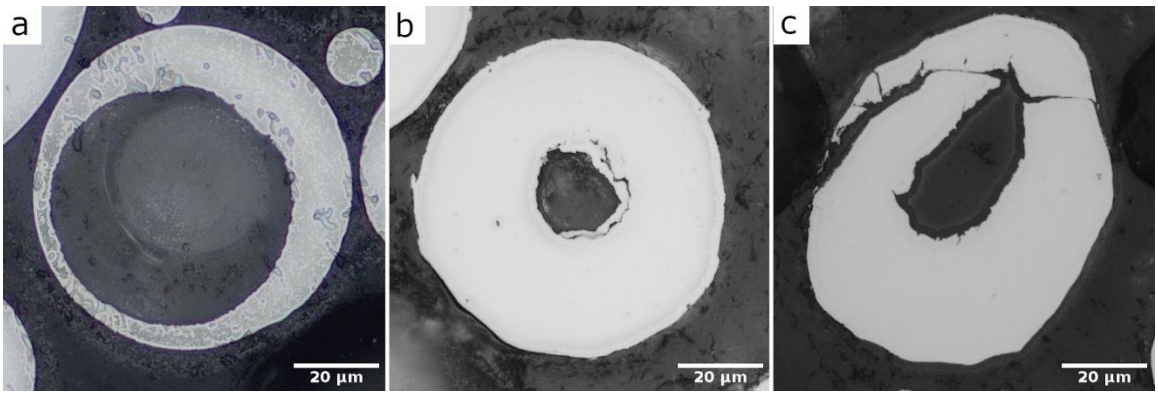

Figure 3.6. Several examples of damaged/degraded powder particles revealed by cross-sectioning. a) surface connected pore in b1 powder. b) internal pore in b30 powder. c) crushed pore in t30 powder.

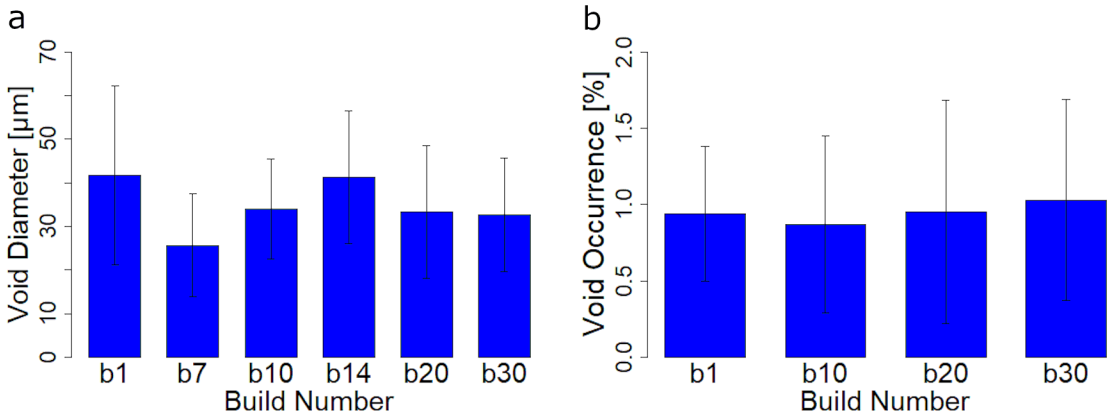

Figure 3.7. Charts showing void measurements for selected builds: (a) calculated true void diameters and (b) void occurrence rate.

Table 3.1. Average measured void diameters and calculated true void diameters for selected powder samples.

Sample	Average Void Diameter (μm)	Calculated True Diameter (μm)	Number of Voids Measured
b1	34.0 ± 16.7	41.6 ± 20.5	12
b7	20.9 ± 9.6	25.6 ± 11.8	18
b10	27.7 ± 9.4	33.9 ± 11.5	21
b14	33.7 ± 12.4	41.2 ± 15.2	35
b20	27.2 ± 12.4	33.3 ± 15.2	20
b30	26.7 ± 10.6	32.7 ± 13.0	19

Table 3.2. Average measured void diameters and calculated true void diameters for selected powder samples.

Sample	Particle Count	Void Count	Percent of Particles with Void
b1	2021	19	0.94 ± 0.44
b10	3922	34	0.87 ± 0.58
b20	3475	33	0.95 ± 0.73
b30	3384	35	1.03 ± 0.66

3.2 NANOINDENTATION

An example of the indentation array used for the hardness analysis of the titanium powder particles is shown in Figure 3.8. Representative hardness profiles for selected particles of the heat-treated powder (a1p5) and the reused powder from build 30 (b30p19) are shown in Figure 3.9. It is important to note that the data for these two particles is presented on different hardness ranges to accommodate the different peak hardness of the two conditions. There is a clear trend evident in both graphs reflecting the larger indentation hardness near the surface. The particles from the heat-treated powder clearly exhibited the largest near-surface hardness.

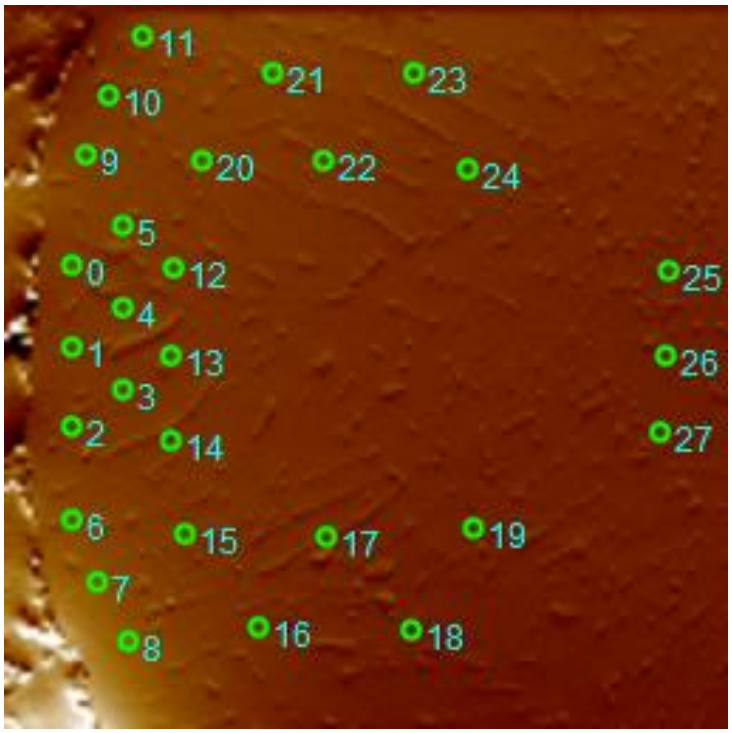

Figure 3.8. Typical indentation array used to measure surface-to-core hardness.

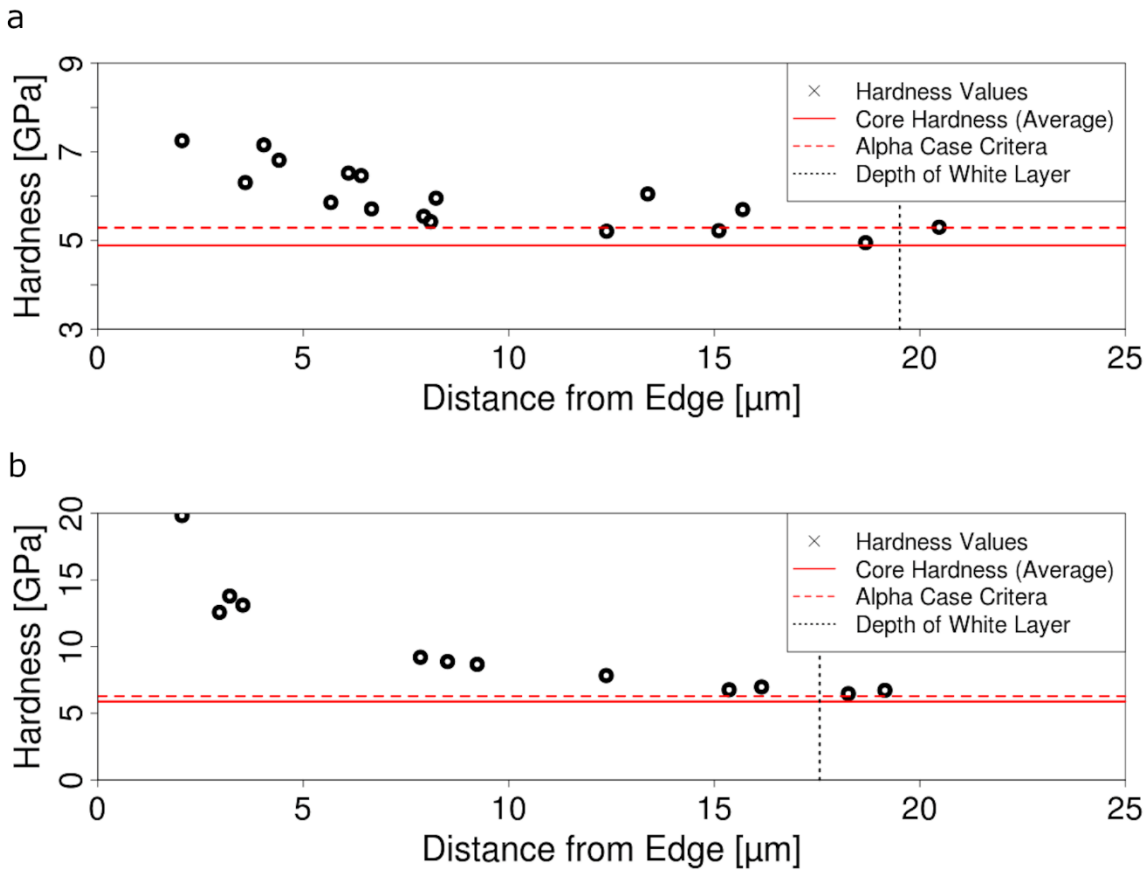

Figure 3.9. Hardness profile plots from particles (a) b30p19 and (b) a1p5

For the heat-treated powder, three particles were selected for analysis based on the clarity of the white layer visible in the tint-etched condition. A photomicrograph of one of these particles is shown in Figure 3.10. All three particles had significant surface hardening, with surface values being up to 15 GPa higher than the core. Similarly, a photomicrograph of one particle of the reused powder from b30 after the tint-etch process is presented in Figure 3.10. A visible white layer is also evident. The average surface hardness for each particle was taken from the indents measured between 2.5 and 5 µm from the edge of the particle, which is well within the white layer. The measured values for the average core hardness and surface hardness of these particles is presented in Table 2.3, along with the hardness differentials. According to the measured hardness, the hardness differentials with regards to the core for particle a1p4, a1p5, and a1p6 were 7.3, 5.4 and

6.6 GPa, respectively. All these values are >> 0.4 GPa hardness differential required for establishing the presence of an alpha-case.

Surface hardening in the reused powder was evident, although not to the extent of that in the alpha-case powder. The core hardness gave an average of 5.0 ± 0.2 GPa over the 30 builds, with no trend. However, the surface hardness increased from 4.7 ± 0.45 to 6.8 ± 0.4 GPa, which represents a significant increase over the 30 builds. Particle b1p2 from the b1 powder sample (virgin powder) showed a core hardness of 4.9 ± 0.3 GPa, with no change in hardness from the core to the edge. Likewise, particles b10p15 and b10p19 did not show significant surface hardening. Particle b20 p14 showed a surface hardness of 5.6 ± 0.2 GPa, and a core hardness of 5.2 ± 0.3 GPa. This represents a hardness differential of 0.4 GPa, just at the alpha-case threshold. Particle b30p19 showed a surface hardness of 6.8 ± 0.4 GPa, and a core hardness of 4.9 ± 0.2 GPa. This represents a hardness differential of 1.9 GPa, sufficient to classify as alpha-case. The measured hardness values for particle b30p19 dropped to within 0.4 GPa of the average core hardness at approximately 20 μm from the surface. The results are summarized in Table 3.3. Summary of average surface and core hardness for selected particles

The hardness distributions, as well as the average surface and core values were also evaluated for particles from the accelerated PRS study. These particles were selected based on optical micrographs for having microstructures similar to the virgin powder and evidence of mechanical deformation. A comparison of the average surface and core hardness for these particles is shown in Figure 3.11. None of the particles from the accelerated PRS powder sample showed surface hardening in excess of 0.4 GPa from the average core hardness. Average surface hardness values were measured within 0.4 GPa of the core values in all cases.

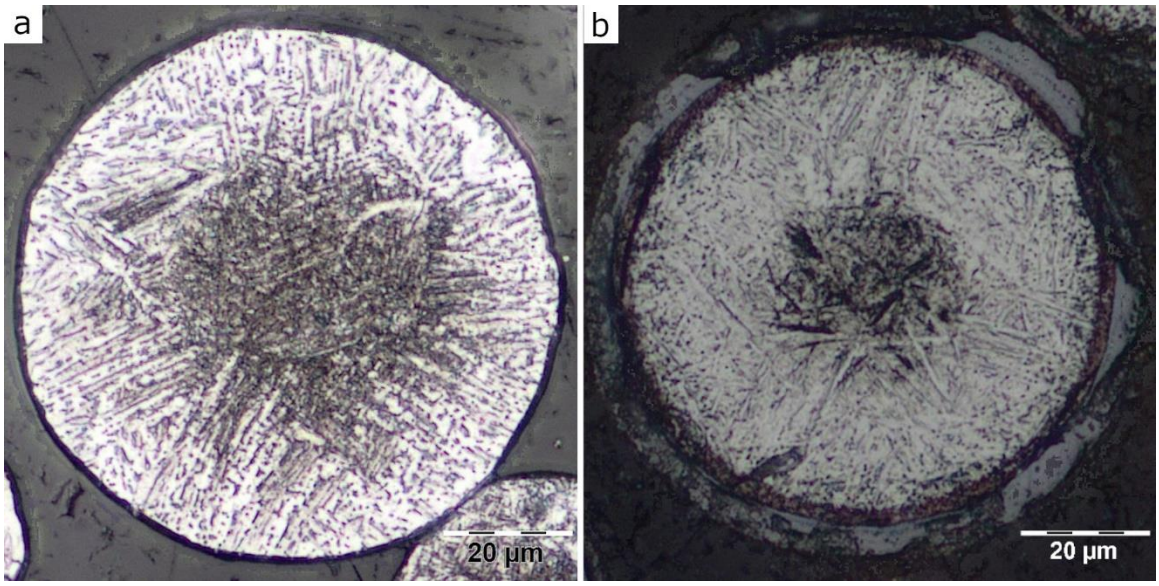

Figure 3.10. Photomicrographs of particles (a) a1p5 and (b) b30p19, etched with Kroll's and ABF to reveal the alpha case.

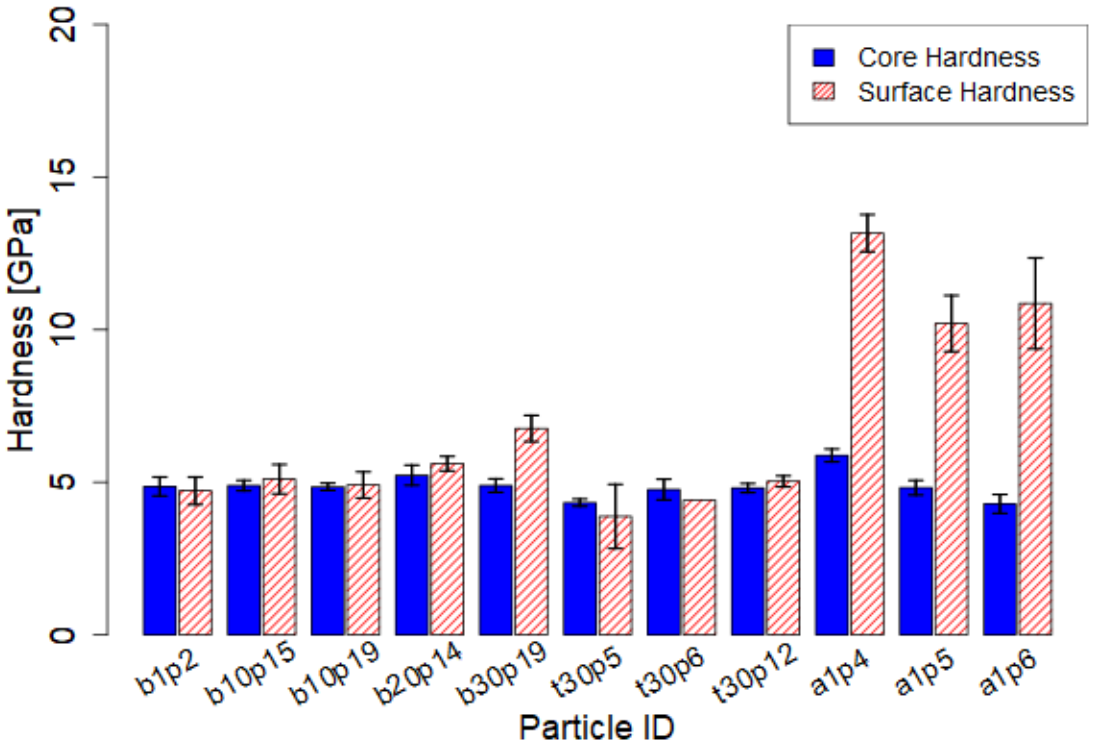

Figure 3.11. Chart showing the average surface and core hardness for each measured particle

Table 3.3. Summary of average surface and core hardness for selected particles

Sample	Average Surface Hardness[1] (GPa)	Average Core Hardness[2] (GPa)	Hardness Differential (GPa)
b1p2	4.72 ± 0.45	4.86 ± 0.32	-0.14 ± 0.55
b10p15	5.10 ± 0.48	4.89 ± 0.17	0.21 ± 0.51
b10p19	4.91 ± 0.43	4.85 ± 0.12	0.06 ± 0.45
b20p14	5.61 ± 0.24	5.23 ± 0.33	0.39 ± 0.40
b30p19	6.76 ± 0.43	4.89 ± 0.22	1.87 ± 0.48
t30p5	3.88 ± 1.05	4.33 ± 0.12	-0.45 ± 1.06
t30p6	4.41*	4.76 ± 0.34	-0.35*
t30p12	5.03 ± 0.18	4.81 ± 0.15	0.22 ± 0.24
a1p4	13.16 ± 0.61	5.88 ± 0.21	7.27 ± 0.65
a1p5	10.20 ± 0.92	4.82 ± 0.24	5.38 ± 0.95
a1p6	10.86 ± 1.49	4.29 ± 0.31	6.56 ± 1.53

[1]Average of indents from 2.5μm - 5μm of the surface
[2]Average of 5 indents
*No statistics are available

Table 3.4. Depth of white layer on particle cross-sections as measured optically

Sample	White Layer Depth (μm)
a1p2	22.8 ± 2.0
a1p4	17.6 ± 2.5
a1p5	20.5 ± 1.4
a1p6	18.9 ± 2.0
b30p19	19.5 ± 2.6

3.3 SEM/EDS

EDS line scans from the surface of the alpha-case particles to the core showed significant changes in oxygen signal intensity, with the signal counts per second being up to three times higher at the surface as compared to the core. The oxygen signal intensity drops rapidly towards the center of the particle, leveling off to values similar to those at the core by approximately 15 μm from the surface in the particles measured. An example for a representative particle is shown in Figure 3.12. Direct calculation of oxygen concentration cannot be determined by EDS due to limitations of the approach as well as complications due to energy peak overlap between oxygen and vanadium. Although the presence of an alpha case layer in the reused powder is strongly suggested from the tint etch and hardness measurements (as shown in Figure 3.10 and Figure 3.11), there were no changes in oxygen signal intensity detected between the surface and the core. Similarly, the EDS analysis was also performed on the powder particles of the PRS study, with no discernible change in signal intensity from the surface to the core of these particles.

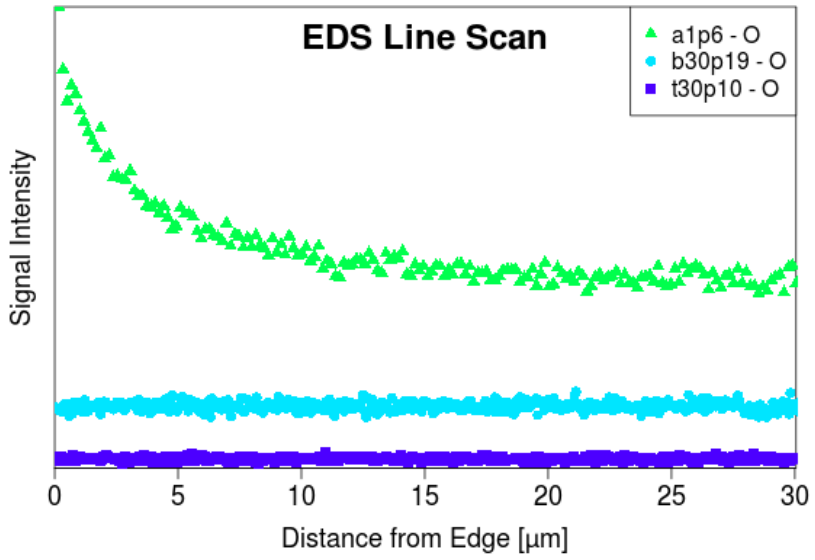

Figure 3.12. Representative EDS spectra from the a1, b30, and t30 powder samples (stacked), showing oxygen signal intensity at the surface of the particles

3.4 ToF-SIMS

Radial profile scans of the alpha-case particles showed increasing signal intensity towards the edge of the particle, commentate to the changes in signal intensity observed with EDS. The trend is visible in the data collected after 2 minutes and 4 minutes of sputtering, though the trend is more clear after 4 minutes. A graph showing the oxygen signal intensity as a function of distance from the particle center is shown in Figure 3.13.

Counter to expectations, the reused powder appears to show a decrease in signal intensity towards the edge of the particle, as shown in the graphs in Figure 3.13(a-b). This decrease in signal intensity is attributed to a deposition of carbon onto the edge of the particle during the sputter process. Graphs showing the carbon signal is shown in Figure 3.13(c-d).

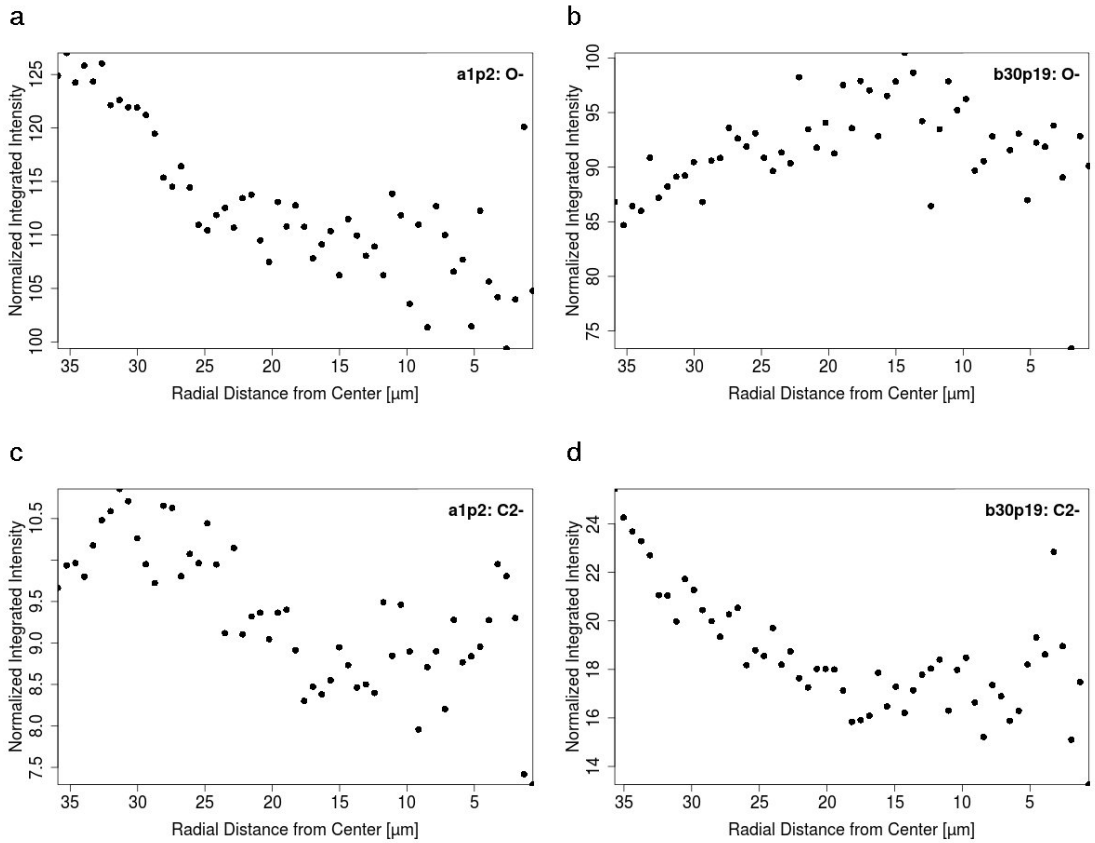

Figure 3.13. Representative EDS spectra from the a1, b30, and t30 powder samples (stacked), showing oxygen signal intensity at the surface of the particles

3.5 OTHER CONTAMINANTS

Several particles were observed to exhibit a white etching layer and had surface hardening in excess of the 0.4 GPa requirement for alpha case, however it was determined that the hardening was caused by contamination by elements other than oxygen. Particles b30p9 and b30p15 were two such particles; the microstructure of these particles is shown in Figure Figure 3.14, and the results of nanoindentation and EDS in Figures 3.19-21. For b30p9, the white layer formed a distinct partial “shell” on one edge of the particle, with the texture of the white layer bring more nodular than what was observe in other particles. This particle had slight surface hardening, up to ~6.5 GPa near the surface in the region of the white layer. EDS revealed that this region was distinctly rich in iron, nickel, and chromium, elements which are also found in the steel build plate used during the build process. The white layer in particle b30p15 was also more distinct than what was observed in particle b30p19, although a slight gradient in color was observed extending below the white layer region. This particle showed surface hardening similar to that seen in particle b30p19, however in this particle there was observed a high concentration of aluminum at the surface of the particle. These were the only two particles observed showing raised concentrations of elements other than oxygen.

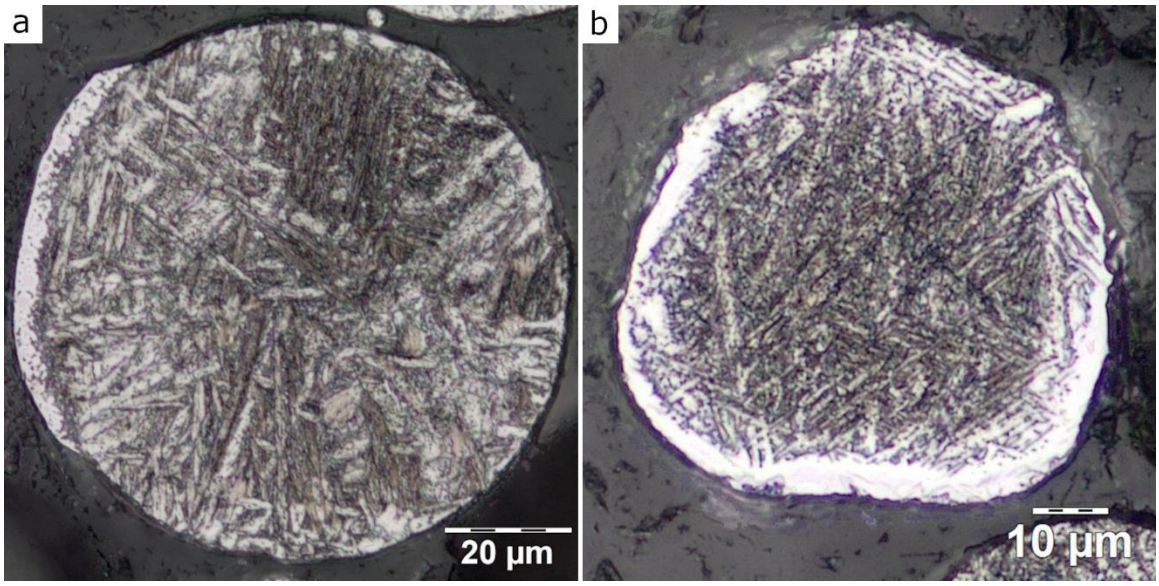

Figure 3.14. Photomicrographs showing observed white layer on (a) b30p9 and (b) b30p15. Etched with Kroll's and ABF.

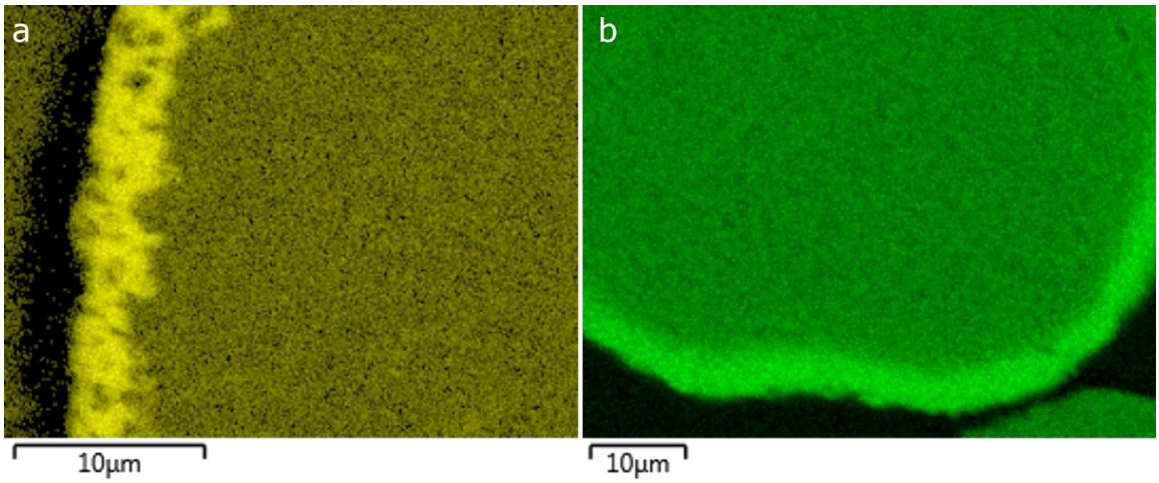

Figure 3.15. EDS maps showing spatial changes in signal intensity for (a) nickel in b30p9 and (b) aluminum in b30p15

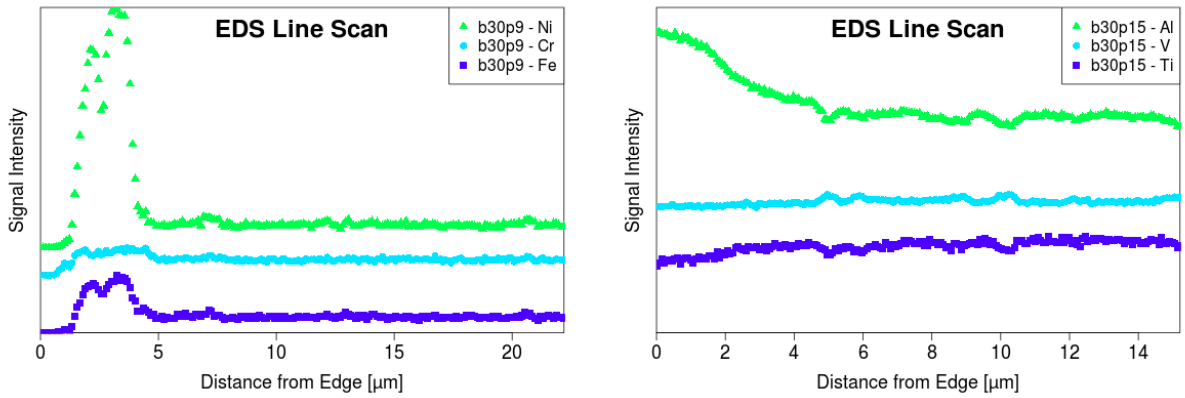

Figure 3.16. Nanoindentation hardness profiles for particles b30p9 and b30p15, showing surface hardening in both particles

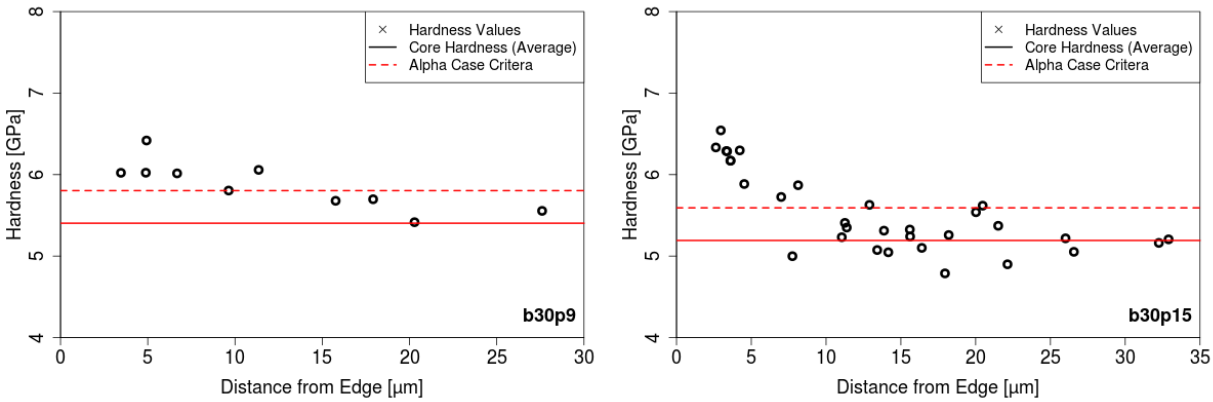

Figure 3.17. Photomicrographs showing observed white layer on (a) b30p9 and (b) b30p15. Etched with Kroll's and ABF.

Chapter 4. DISCUSSION

4.1 OXYGEN CONTENT

The primary objective of this investigation was to evaluate the changes in properties of metal powder that occur over multiple build cycles in EBM with Ti6Al4V and to identify the primary contributing factors. According to results from the evaluation of microstructure, hardness profiles and composition, the findings suggest that oxygen diffusion occurs to the powder during the thermal cycles in EBM AM, which manifests as an alpha-case layer that extends from the surface inwards. The identification of alpha-case on the particles is a result of two different and independent measures, including the observation of oxygen contamination by the ABF tint etch, and identification of near-surface hardening through nanoindentation hardness testing. Surprisingly, substantial oxygen ingress in the feedstock was observed despite the use of vacuum in the EBM processing.

Although both the reused and alpha-case treated powders experienced similar levels of heat exposure ($T \geq 700°C$), the reused powder underwent heating under vacuum while the a1 powder was exposed to air. The oxygen was much greater in the heat-treated powder (a1), enabling significantly more surface hardening as evident in Figure 3.9. This was also evident optically by the presence of a more substantial and distinct oxide layer on the a1 powder particles. Thus, the lower extent of hardening in the heavily reused (b30) powder was expected due to the lower concentration of oxygen exposure. Furthermore, the individual particles of the reused powder experienced different thermal and chemical environments depending on their location within the build chamber, differences in handling and their history in the mixing process. In fact, not all the b30 particles were expected to exhibit hardening. Hence, the findings presented here do not reflect the state of the reused powder globally, but rather present possible transformation routes that

individual particles may take. Therefore, case hardening of the particles by oxygen diffusion is presented as a possibility in the powder, rather than a global certainty applicable to all particles. The particle mixing protocol and the proximity of the particles relative to the part boundaries in the build cycles are important contributions to the degradation process.

Although efforts were made to identify oxygen in the b30 powder via EDS and ToF-SIMS methods, these approaches proved unreliable in detecting the differences in oxygen concentration that had apparently occurred. Despite the tint etching and hardness measurements suggesting the presence of an alpha case layer on the b30 powder particles, it was not substantial enough to be observed from the oxygen signal intensity in the EDS line scans. Yet, this does not necessarily rule out the presence of an alpha case layer. Recent studies have suggested that a drastic change in mechanical properties occurs in titanium at an oxygen content of around 0.3 wt% [27-29]. Assuming that the oxygen concentration near the surface of the powder is at or around this level, it is close to the minimum detection limits for light elements on most EDS systems. This is further complicated due to the overlap between the oxygen K peak at 0.523 eV and the vanadium Kα peak at 0.511 eV [39]. Since vanadium is present in the particles at a nominal composition of 4 wt%, it is possible that the signal from the vanadium overwhelms small changes in the oxygen signal for the reused (b30) powder. This idea is supported by the EDS results of the heat-treated powder (a1) which leveled off to a consistent baseline before the hardness values passed below the alpha-case threshold. Apparently, the concentration of oxygen in the metal was sufficient to induce hardening of the metal but was below the detection limits by EDS. ToF-SIMS may have the capability of detecting the small changes in oxygen in the particles, but efforts to do so were hampered by the method of preparation of the samples. In order to obtain cross-sections of the powder to identify target particles, the powder had to be mounted in a supportive medium, in this case epoxy resin.

Additionally, due to the shallow penetration of the ToF-SIMS analysis beam, the passive oxide layer on the particles surface had to be removed prior to analysis, and in an environment where a new oxide layer could not form. However, the only method available to remove the oxide layer - sputtering the surface of the sample with Ar - resulted in carbon in the epoxy being sputtered and deposited on the edges of the particles that were being analyzed. This carbon layer obscured the underlying material and resulted in inaccurate measurements. Unless some method is devised to remove the passive oxide layer without depositing more material, the ToF-SIMS technique will not be able to provide accurate or reliable measurements.

4.2 ABF Tint Etch

The ABF tint etch is a test often used to detect the presence of an alpha-case layer on titanium that has undergone heat treatments [29]. It is important to note, however, that other etch interactions can create lighter etching regions, and so the presence of a white surface layer is not by itself sufficient evidence for confirmation of an alpha-case. As such, it is necessary to confirm the presence of the alpha-case through a secondary test, and most ideally a quantifiable measurement. For this reason, nanoindentation hardness testing was employed to examine hardness gradients from the particle surface that are related to either oxidation or another aspect of the processing.

One finding of importance is the relative agreement between the microstructure and hardness measurements, and their synergy. For instance, in all the particles with observed white layer and surface hardening, the subsurface hardness decreased below the alpha-case criteria limit at distances that were largely consistent with the measured depth of the white layer on those particles. That consistency is evident in the hardness profiles presented in Figure 3.9 for the selected alpha-case and the reused powder particles. It not only provides supporting evidence that the white layer is indicative of alpha-case, but also suggests that the ABF tint offers an effective route for

quantifying the depth of the alpha case. Nevertheless, the ABF tint etch alone is not sufficient to reliably claim alpha-case in all cases. Several particles were observed to exhibit a white layer but did not exhibit surface hardening. There were also particles that exhibited a prominent white layer and surface hardening, but the source of the hardening originated from sources other than oxygen. Admittedly, the estimated alpha-case depths may not represent true depths due to the random sectioning of the powder and potential deviation from the true-midplane. Depending on where the particle was sectioned, the skew of the surface relative to the polish plane can exaggerate the depth measurement, with greater exaggerations resulting from shallower cross-sections.

4.3 Effects of Deformation

The absence of hardening in the accelerated PRS powder (t30) suggests that mechanical deformation does not cause significant surface hardening in Ti6Al4V powder particles. In fact, most of the t30 particles showed lower hardness near the surface than at the core. This could be a result of the limitations of the indentation approach near the surface of cross-sectioned particles, causing the indenter to penetrate farther and giving the impression of softer material. It could also be a function of the limited depth of the hardened layer induced by deformation. The t30 powder was virgin powder introduced directly to the PRS. It did not undergo a heating process sufficient to allow significant oxygen diffusion into the metal. Since particles were selected for characterization based on the severity of their deformation, it is assumed that the examined particles represent worst-case scenarios. Therefore, since none of the particles showed signs of hardening, the work-hardening in particles with less-substantial signs of deformation would be equally minimal. Also noteworthy, the average void diameter and frequency of occurrence in the particles was not observed to change with reuse time. As such, crushing of particles in the PRS with internal voids is not a significant factor.

4.4 Potential Contamination Sources

Previous work by Tang et al. [6] attributed the increase in oxygen content of Ti6Al4V powder to oxygen pickup that occurs when it is exposed to air during the PRS, mixing, and sieving steps. It is most likely that the main source of oxygen is actually water vapor in the air. When exposed, water molecules adsorb onto the surface of the powder particles. These molecules dissociate during the heating cycles in the EBM chamber, allowing the oxygen to penetrate the metal. This process has been previously shown to occur during gas tungsten arc (GTA) welding of titanium alloys produced using powder metallurgy [40]. Another potential source of oxygen is the passive oxide layer that forms spontaneously on the surface of titanium metal when exposed to air. Although only a few nanometers thick, progressive heating cycles and air exposure could cause the oxide layer to diffuse inward and reform periodically. That comment is speculative and requires further support.

The contamination in particles b30p9 and b30p15 is thought to originate from sources within the build chamber during the build process. For particle b30p9, the major contaminates were iron, nickel, and chromium. Previous projects using this machine at the university have shown that during the first layers of a build, the electron beam penetrates far enough to heat the steel build plate to the point where it partially fuses with the melt pool on top of it. This allows the steel base plate to partially alloy with the material being printed on top. It is likely that this particle picked up this contamination from the build plate at some point during the earlier builds. This is an important consideration for powder reuse as it introduces an avenue for metallic contaminates in the powder, depending on what material is used for the build plate. Iron in particular is detrimental for titanium as it promotes the formation of an Fe-β phase in the material.

The origin of the aluminum contamination in particle b30p15 is less clear. It is known that the lower melting point of aluminum causes it to preferentially vaporize during the melt process. This is evidenced by the slightly lower aluminum content in the built parts as compared to the powder. It is possible that aluminum was vaporized from the melt pool by the heat of the beam and deposited on nearby unmelted powder particles. This would result in particles with increased aluminum content at the surface, but no other large changes in chemistry, as was observed in particle b30p15. This process however is unconfirmed and so far just speculation. A process such as this would not be a significant concern for powder reuse beyond how it affects the shape and flowability of the powder, as is not capturing external material in the powder.

4.5 REPRODUCIBILITY

Despite the value of the findings in providing a fundamental understanding of the changes in powder particles with reuse in EBM with Ti6Al4V, there are limitations to the effort that are important to consider. Primarily, the techniques used in this study only provide information on the individual particles measured. Thus drawing broader conclusions regarding the bulk properties of the powder are not recommended as they are a function of the individual powder handling procedures used, the manner in which additional powder is added incrementally in successive builds, etc. These are important issues that remain for future studies.

Chapter 5. NANOINDENTATION REPEATABILITY

It was noted during the investigation that the values of the core hardness were drifting over time, even for the same sample measured on the same machine several weeks apart. It was suspected that the indenter tip was being worn down due to the high usage of the machine during this timeframe. In order to track this wear, hardness measurements were taken on a fused silica quartz standard at the start of each measurement session. Hardness readings from this quartz standard are plotted over time in Figure 5.1. It was quickly observed that the measured hardness of the quartz standard was increasing over time, and was well above the nominal standard hardness of 9.25GPa. At the end of July 2019 a calibration was performed on the system in response to the drifting values. Subsequent measurements after the recalibration were observed to be in line with the expected value, within a margin of error. To rule out sample variability of the quartz standard, hardness measurement arrays were taken both locally and broadly across the surface of the standard. Five measurements were taken roughly in the center of the sample with an indent spacing of 10μm. Five more indents were taken, spread out across the surface of the sample. The variance of measured hardness values in one location was determined to be 1%, with a 3% variance across the entire sample. Is was concluded that the hardness of the quartz was reliably consistent and independent of location.

The reason for this variation in the data over time is assumed to be a change in the geometry of the indenter tip due to wear from excessive use. It would be expected that as the tip became worn and rounded, the force required to achieve a certain penetration depth would increase, giving the impression of a harder material. Indeed, it was observed that the values obtained from the quartz sample trended upwards over time before the calibration event.

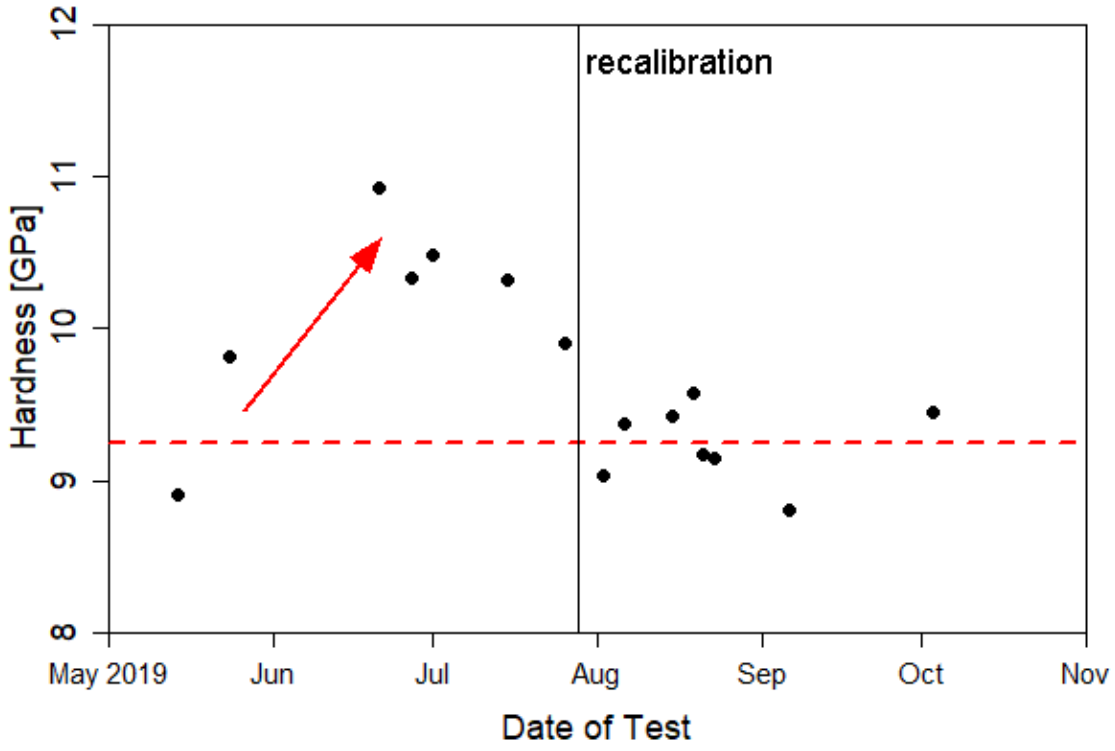

Figure 5.1. Plot showing the measured hardness of a fused silica standard used for checking the nanoindentation machine. The dashed red line denotes the nominal hardness of 9.25 Gpa. Note the upward trend between May and July, indicated by the red arrow. A recalibration of the machine occurred at the end of July, indicated by the solid black line.

For this reason, while values for nanoindentation hardness are given in this work, they are only used for comparison with other measurements taken on the same day. Since single particle hardness profiles were taken in single machine runs, they are considered valid for comparing surface-to-core hardness, however comparisons between different particles are intentionally omitted. It may be possible to normalize the values against prerecorded quartz measurements, however in this case insufficient data was collected to make this effort. It is also possible to apply new tip geometry calibrations to previously taken data, however there still exists some margin for error if the tip geometry is changing rapidly enough, or if calibrations are not made often enough.

Chapter 6. CONCLUSIONS

An experimental evaluation of Ti6Al4V metal powder particles was conducted over 30 build cycles of Electron Beam Melting (EBM) additive manufacturing (AM). For comparison, powder particles were also analyzed after an alpha-case heat treatment (control) and after accelerated mechanical processing by powder recovery system (PRS). Based on morphological, microstructural, mechanical, and chemical analyses performed on cross-sectioned powder particles, the following conclusions are drawn:

1) The thermal cycling inherent to the EBM-PBF process causes coarsening of the particle microstructure. The extent of coarsening depends heavily on the specific thermal history of the individual particles, which depends on their location in the machine and with respect to the melt pool and part. Heavily reused powder exhibits a broad range of microstructures and thus a commensurately broad range of mechanical properties.

2) The effect of oxygen diffusion in the powder is assumed to be cumulative with reuse times, with additional oxygen being introduced every time the powder is removed from the build chamber. Significant powder reuse can lead to the development of an oxygen rich case layer on a portion of the particles, which will depend on the volume of powder used in the build cycle and the particle proximity to heat.

3) Surface hardening of the powder particles occurs during powder reuse. The hardening appears to result from contamination of the powder via external sources, with oxygen ingress representing one possible mechanism. The exact mechanism was not identified.

4) Work hardening by mechanical deformation of the powder particles is not a significant factor in powder reuse. However, the mechanical deformation itself is an important factor in other aspects

of powder reuse. Changes in powder morphology will undoubtedly affect the flowability and spreadability of the powder in the machine.

5) In EBM AM with Ti6Al4V and other powders that develop spontaneous passive oxide layers, it is essential to monitor/manage powder oxidation and its detrimental effects on the resultant built material. Concerted efforts should be made to develop systems that prevent powder exposure to oxygen sources, or to develop methods (chemical or physical) of removing the surface oxygen sources prior to each build.

BIBLIOGRAPHY

[1] ASTM, "ISO/ASTM 52900:2015(E) Standard Terminology for Additive Manufacturing – General Principles – Terminology," *ASTM Int.*, vol. i, pp. 1–9, 2015, doi: 10.1520/F2792-12A.2.

[2] T. DebRoy *et al.*, "Additive manufacturing of metallic components – Process, structure and properties," *Prog. Mater. Sci.*, vol. 92, pp. 112–224, 2018, doi: 10.1016/j.pmatsci.2017.10.001.

[3] D. L. Bourell, "Perspectives on Additive Manufacturing," *Annu. Rev. Mater. Res.*, vol. 46, no. 1, pp. 1–18, 2016, doi: 10.1146/annurev-matsci-070115-031606.

[4] Y. Zhai, D. A. Lados, and J. L. Lagoy, "Additive Manufacturing: Making imagination the major Limitation," *Jom*, vol. 66, no. 5, pp. 808–816, 2014, doi: 10.1007/s11837-014-0886-2.

[5] Y. Sun, M. Aindow, and R. J. Hebert, "The effect of recycling on the oxygen distribution in Ti-6Al-4V powder for additive manufacturing," *Mater. High Temp.*, vol. 35, no. 1–3, pp. 217–224, May 2018, doi: 10.1080/09603409.2017.1389133.

[6] H. P. Tang, M. Qian, N. Liu, X. Z. Zhang, G. Y. Yang, and J. Wang, "Effect of Powder Reuse Times on Additive Manufacturing of Ti-6Al-4V by Selective Electron Beam Melting," *Jom*, vol. 67, no. 3, pp. 555–563, 2015, doi: 10.1007/s11837-015-1300-4.

[7] P. Nandwana *et al.*, "Recyclability Study on Inconel 718 and Ti-6Al-4V Powders for Use in Electron Beam Melting," *Metall. Mater. Trans. B*, vol. 47, no. 1, pp. 754–762, Feb. 2016, doi: 10.1007/s11663-015-0477-9.

[8] Renishaw, "Investigating the effects of multiple re-use of Ti6Al4V powder in additive manufacturing," *Renishaw*, pp. 1–10, 2016.

[9] V. Petrovic and R. Niñerola, "Powder recyclability in electron beam melting for aeronautical use," *Aircr. Eng. Aerosp. Technol.*, vol. 87, no. 2, pp. 147–155, Mar. 2015, doi: 10.1108/AEAT-11-2013-0212.

[10] G. Lütjering, "Influence of processing on microstructure and mechanical properties of (α + β) titanium alloys," *Mater. Sci. Eng. A*, vol. 243, no. 1–2, pp. 32–45, 1998, doi: 10.1016/s0921-5093(97)00778-8.

[11] X. Zhao *et al.*, “Comparison of the microstructures and mechanical properties of Ti-6Al-4V fabricated by selective laser melting and electron beam melting,” *Mater. Des.*, vol. 95, pp. 21–31, Apr. 2016, doi: 10.1016/j.matdes.2015.12.135.

[12] T. M. Mower and M. J. Long, “Mechanical behavior of additive manufactured, powder-bed laser-fused materials,” *Mater. Sci. Eng. A*, vol. 651, pp. 198–213, Jan. 2016, doi: 10.1016/j.msea.2015.10.068.

[13] M. Svensson and U. Ackelid, “Titanium Alloys Manufactured with Electron Beam Melting Mechanical and Chemical Properties,” in *Materials & Processes for Medical Devices Conference 2009*, 2009, pp. 189–194.

[14] J. J. Lewandowski and M. Seifi, “Metal Additive Manufacturing: A Review of Mechanical Properties,” *Annu. Rev. Mater. Res.*, vol. 46, no. 1, pp. 151–186, May 2016, doi: 10.1146/annurev-matsci-070115-032024.

[15] J. Karlsson, M. Norell, U. Ackelid, H. Engqvist, and J. Lausmaa, “Surface oxidation behavior of Ti-6Al-4V manufactured by Electron Beam Melting (EBM®),” *J. Manuf. Process.*, vol. 17, pp. 120–126, 2015, doi: 10.1016/j.jmapro.2014.08.005.

[16] T. A. Parthasarathy, W. J. Porter, S. Boone, R. John, and P. Martin, “Life prediction under tension of titanium alloys that develop an oxygenated brittle case during use,” *Scr. Mater.*, vol. 65, no. 5, pp. 420–423, 2011, doi: 10.1016/j.scriptamat.2011.05.025.

[17] S. Zabler, “Interstitial Oxygen diffusion hardening - A practical route for the surface protection of titanium,” *Mater. Charact.*, vol. 62, no. 12, pp. 1205–1213, 2011, doi: 10.1016/j.matchar.2011.10.012.

[18] C. Wei *et al.*, “Microstructural and property evolution of Ti6Al4V powders with the number of usage in additive manufacturing by electron beam melting,” *Mater. Lett.*, vol. 221, pp. 111–114, Jun. 2018, doi: 10.1016/j.matlet.2018.03.124.

[19] V. V. Popov, A. Katz-Demyanetz, A. Garkun, and M. Bamberger, “The effect of powder recycling on the mechanical properties and microstructure of electron beam melted Ti-6Al-4 V specimens,” *Addit. Manuf.*, vol. 22, pp. 834–843, Aug. 2018, doi: 10.1016/j.addma.2018.06.003.

[20] R. Gaddam, B. Sefer, R. Pederson, and M. L. Antti, “Study of alpha-case depth in Ti-6Al-2Sn-4Zr-2Mo and Ti-6Al-4V,” in *IOP Conference Series: Materials Science and Engineering*, 2013, vol. 48, no. 1, doi: 10.1088/1757-899X/48/1/012002.

[21] K. S. Chan, M. Koike, B. W. Johnson, and T. Okabe, “Modeling of alpha-case formation and its effects on the mechanical properties of titanium alloy castings,” *Metall. Mater. Trans. A Phys. Metall. Mater. Sci.*, vol. 39, no. 1, pp. 171–180, 2008, doi: 10.1007/s11661-007-9406-0.

[22] S. Y. Sung and Y. J. Kim, “Alpha-case formation mechanism on titanium investment castings,” *Mater. Sci. Eng. A*, vol. 405, no. 1–2, pp. 173–177, 2005, doi: 10.1016/j.msea.2005.05.092.

[23] R. G. Keanini, G. K. Watkins, T. Okabe, and M. Koike, “Theoretical study of alpha case formation during titanium casting,” *Metall. Mater. Trans. B Process Metall. Mater. Process. Sci.*, vol. 38, no. 4, pp. 729–732, 2007, doi: 10.1007/s11663-007-9058-x.

[24] V. Deshmukh, R. Kadam, and S. S. Joshi, “Removal of alpha case on titanium alloy surfaces using chemical milling,” *Mach. Sci. Technol.*, vol. 21, no. 2, pp. 257–278, 2017, doi: 10.1080/10910344.2017.1284558.

[25] S.-Y. Sung, B.-S. Han, and Y.-J. Kim, *Formation of Alpha Case Mechanism on Titanium Investment Cast Parts*. InTech, 2012.

[26] P. Zhang and D. R. Trinkle, “A modified embedded atom method potential for interstitial oxygen in titanium,” *Comput. Mater. Sci.*, vol. 124, pp. 204–210, 2016, doi: 10.1016/j.commatsci.2016.07.039.

[27] H. Miura, Y. Itoh, T. Ueamtsu, and K. Sato, “The influence of density and oxygen content on the mechanical properties of injection molded Ti-6Al-4V alloys,” vol. 4, 2010.

[28] P. Krakhmalev, G. Fredriksson, I. Yadroitsava, N. Kazantseva, A. du Plessis, and I. Yadroitsev, “Deformation Behavior and microstructure of Ti6Al4V manufactured by SLM,” *Phys. Procedia*, vol. 83, pp. 778–788, 2016, doi: 10.1016/j.phpro.2016.08.080.

[29] M. J. Donachie, *Titanium: A Technical Guide*, 2nd ed. ASM International, 2000.

[30] H. Conrad, “Effect of interstitial solutes on the strength and ductility of titanium,” *Prog. Mater. Sci.*, vol. 26, no. 2–4, pp. 123–403, 1981, doi: 10.1016/0079-6425(81)90001-3.

[31] S. Ghods *et al.*, “Electron Beam Additive Manufacturing of Ti6Al4V: Evolution of Powder Morphology and Part Microstructure with Powder Reuse,” *Materialia*, vol. 9, no. December 2019, p. 100631, 2020, doi: 10.1016/j.mtla.2020.100631.

[32] F. Pitt and M. Ramulu, “Influence of grain size and microstructure on oxidation rates in titanium alloy Ti-6Al-4V under superplastic forming conditions,” in *Journal of Materials*

Engineering and Performance, 2004, vol. 13, no. 6, pp. 727–734, doi: 10.1361/10599490421394.

[33] ASTM, "ASTM E407-07(2015) Standard Practice for Microetching Metals and Alloys," *ASTM Int.*, pp. 1–22, 2015, doi: 10.1520/E0407-07.2.

[34] ASTM, "ASTM E384 -17 Standard Test Method for Microindentation Hardness of Materials," *ASTM Int.*, pp. 1–40, 2017, doi: 10.1520/E0384-17.

[35] W. C. Oliver and G. M. Pharr, "An improved technique for determining hardness and elastic modulus using load and displacement sensing indentation experiments," *J. Mater. Res.*, vol. 7, no. 6, pp. 1564–1583, 1992, doi: 10.1557/JMR.1992.1564.

[36] SAE, "Ams 4911L," *SAE Aerosp.*, vol. 4970, pp. 1–11, 2011.

[37] P. Carl, "Radial Profile Extended." 2006.

[38] ASM, *Metals Handbook Vol. 7 Atlas of Microstructures of Industrial Alloys*, 8th ed. American Society for Metals, 1972.

[39] D. E. Newbury and N. W. M. Ritchie, "Performing elemental microanalysis with high accuracy and high precision by scanning electron microscopy/silicon drift detector energy-dispersive X-ray spectrometry (SEM/SDD-EDS)," *J. Mater. Sci.*, vol. 50, no. 2, pp. 493–518, 2014, doi: 10.1007/s10853-014-8685-2.

[40] T. R. Muth *et al.*, "Causal factors of weld porosity in gas tungsten arc welding of powder-metallurgy-produced titanium alloys," *Jom*, vol. 65, no. 5, pp. 643–651, 2013, doi: 10.1007/s11837-013-0592-5.

APPENDIX A – POWDER CERTIFICATION

Arcam EBM
A GE Additive Company

Arcam EBM, Krokslätts Fabriker 27A, SE-431 37
Mölndal, Sweden
Tel. +46 31 710 32 00, Fax +46 31 710 32 01
E-mail: info@arcam.com - Internet: www.arcam.com

2017-05-10

Certificate of Analysis No: CA-18-0500

Customer: University of Washington. 3900 E Stevens Way NE, Mech Engr Bldg Rm 132, Seattle, WA 98195, USA.

Material description: Arcam Ti6Al4V powder
Size: 45-106 µm
Specification: UAC065-170510 & ASTM F2924
Part number: 430944

Purchase order No.: PP963186
Batch No.: P1303
Quantity: 50 kg

Powder chemical composition (wt. %)

Element	ASTM F2924	UAC065-170510	Measured	Testing method	Status
Carbon (C)	< 0.08	< 0.08	0.02	ASTM E1941	Conforming
Oxygen (O)	< 0.20	0.11 - 0.20	0.14	ASTM E1409	Conforming
Nitrogen (N)	< 0.05	< 0.05	0.02	ASTM E1409	Conforming
Hydrogen (H)	< 0.015	< 0.015	0.002	ASTM E1447	Conforming
Iron (Fe)	< 0.30	< 0.30	0.20	ASTM E2371	Conforming
Aluminum (Al)	5.50 - 6.75	6.00 - 6.75	6.37	ASTM E2371	Conforming
Vanadium (V)	3.50 - 4.50	3.50 - 4.50	4.01	ASTM E2371	Conforming
Yttrium (Y)	< 0.005	< 0.005	< 0.001	ASTM E2371	Conforming
Others, each	< 0.10	< 0.10	< 0.10	ASTM E2371	Conforming
Others, total	< 0.40	< 0.40	< 0.40	ASTM E2371	Conforming
Titanium (Ti)	Balance	Balance	Balance	ASTM E2371	Conforming

Chemical analysis laboratory: **Luvak Inc.** (722 Main Street, P.O. Box 597, Boylston MA, USA, 01505) Report 0-84823

Powder characterization

Particle size distribution per ASTM B214

Particle Size	% By Mass	% By Mass	Status
< 25 µm*	< 0.7	0.0*	Conforming
25-45 µm*	Report	3.8*	NA
45-106 µm	> 90.0	94.0	Conforming
106-150 µm	Report	2.2	NA
> 150 µm	< 0.2	0.0	Conforming
< 45 µm	< 5.0	3.8	Conforming
> 106 µm	< 5.0	2.2	Conforming

Particle size distribution per ASTM B822 (Coulter® LS 13320)

D10	Report	51 µm	NA
D50	Report	69 µm	NA
D90	Report	99 µm	NA

*Standard ASTM B214 applies to powder sizes 45 microns and higher. The results are for information only.

Description	Required	Measured	Status
Flow rate per ASTM B213			
Flow rate (sec/50 g)	Max. 29	26	Conforming
Apparent density per ASTM B212			
Apparent density (g/cm³)	Min. 2.40	2.49	Conforming
Tap density per ASTM B527			
Tap density (g/cm³)	Min. 2.7	2.8	Conforming

Powder characterization by: **AP&C Inc.** (3765 La Vérendrye, suite 110, Boisbriand, Québec, Canada, J7H 1R8)

☒ Inspection certificate done according to EN 10204 type 3.1. We hereby approve this analysis and certify that the above values conform to the requirements of the purchase order above.

2018-06-13
Date

Catherine Lavoie
Quality department

This powder was specially designed for use on the Arcam EBM systems. Powder characterization requirements are based on Arcam EBM internal processes.

APPENDIX B – FIGURES AND GRAPHS

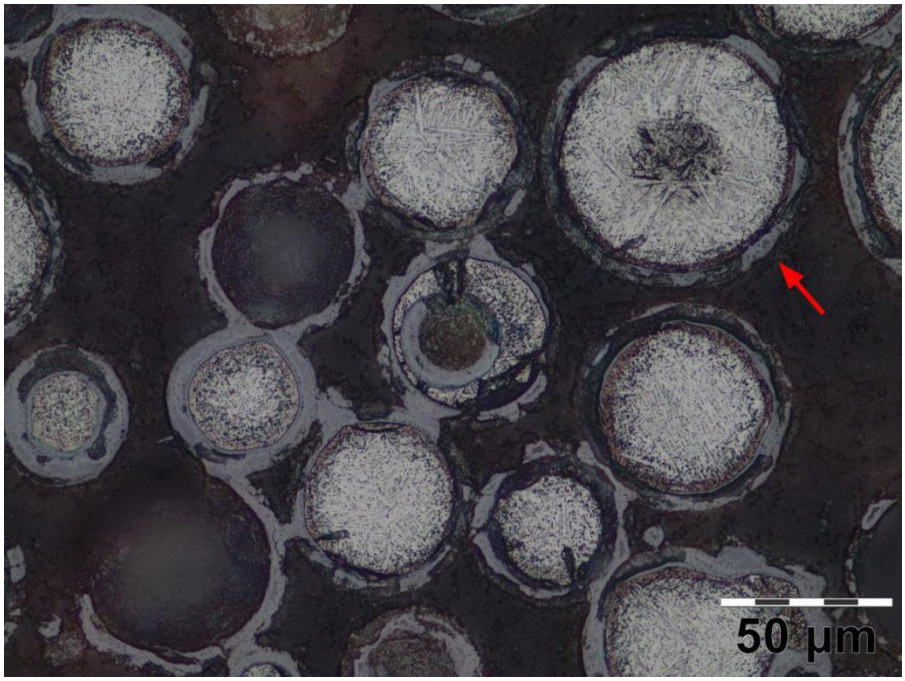

Figure B.1. Photomicrograph showing particle a1p2, indicated by the arrow, etched with Kroll's and ABF

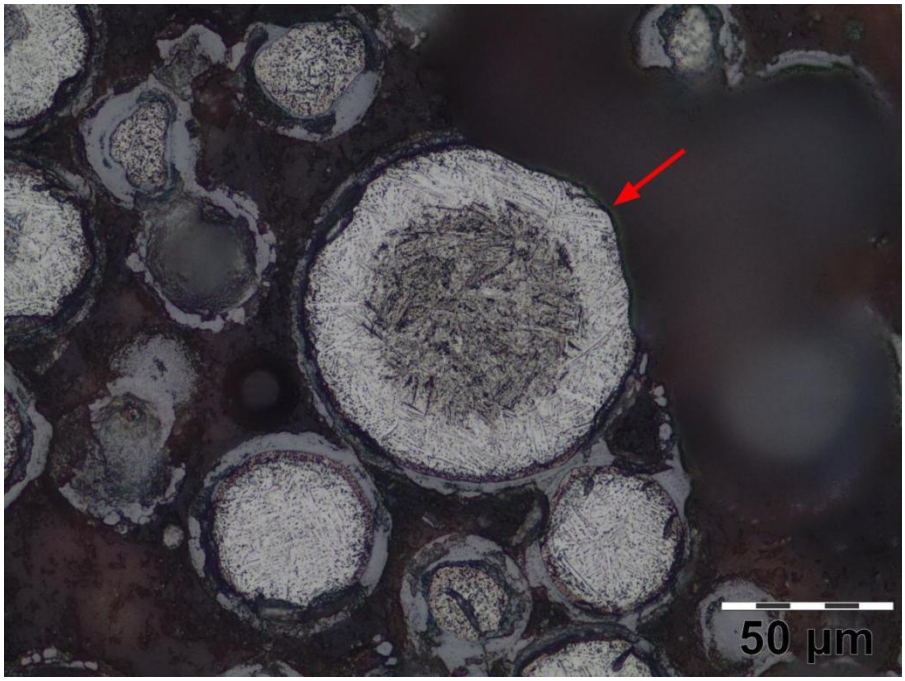

Figure B.2. Photomicrograph showing particle a1p4, indicated by the arrow, etched with Kroll's and ABF

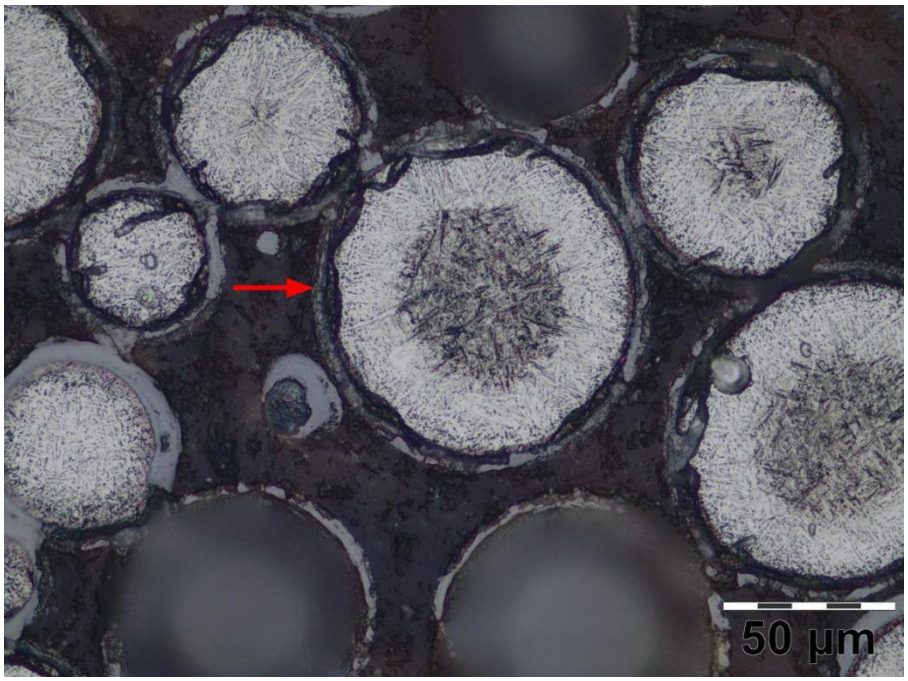

Figure B.3. Photomicrograph showing particle a1p5, indicated by the arrow, etched with Kroll's and ABF

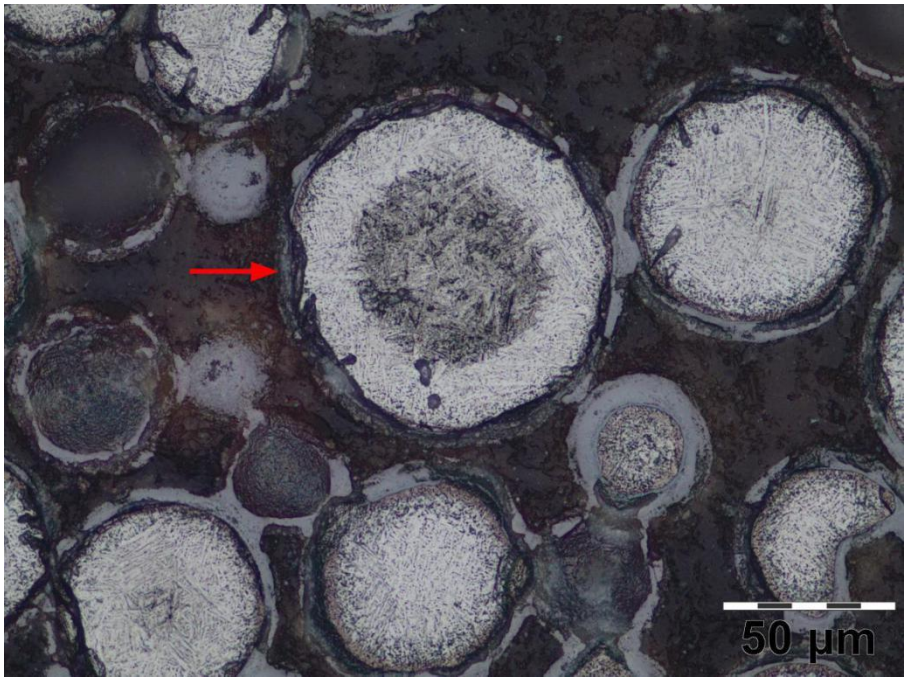

Figure B.4. Photomicrograph showing particle a1p6, indicated by the arrow, etched with Kroll's and ABF

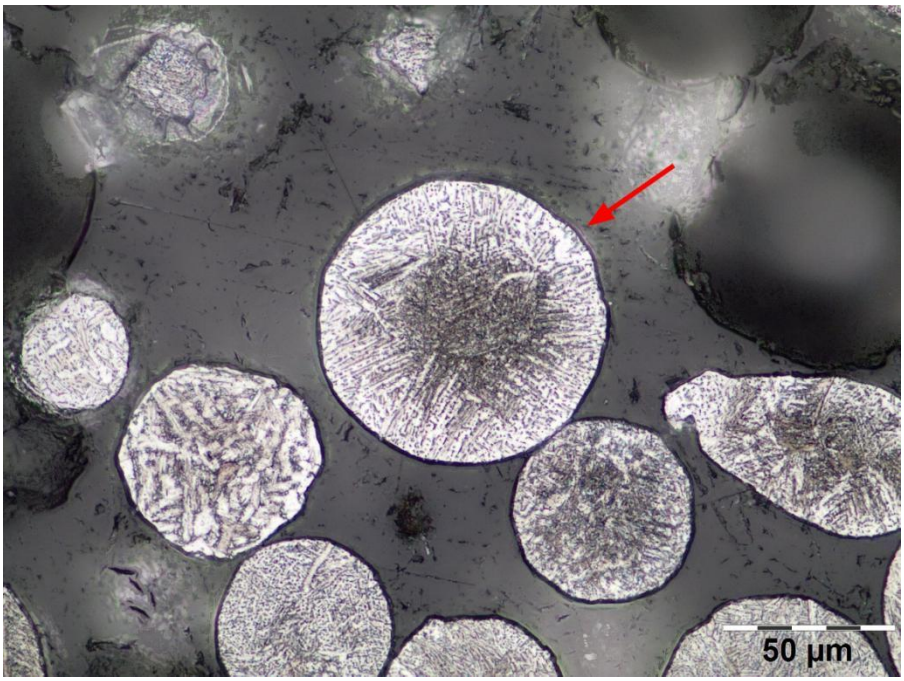

Figure B.5. Photomicrograph showing particle b30 p19, indicated by the arrow, etched with Kroll's and ABF

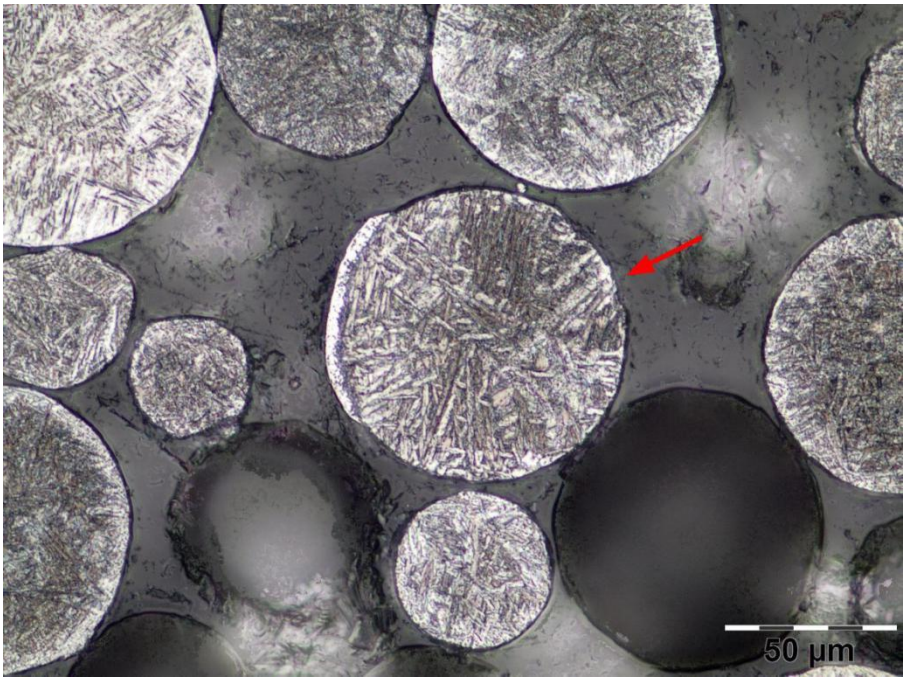

Figure B.6. Photomicrograph showing particle b30p9, indicated by the arrow, etched with Kroll's and ABF

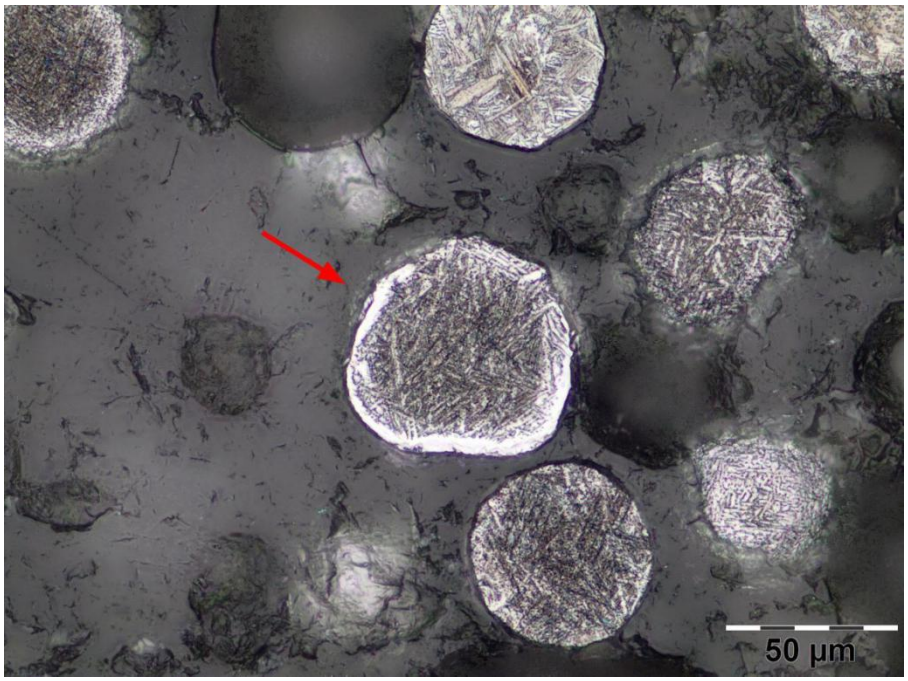

Figure B.7. Photomicrograph showing particle b30p15, indicated by the arrow, etched with Kroll's and ABF

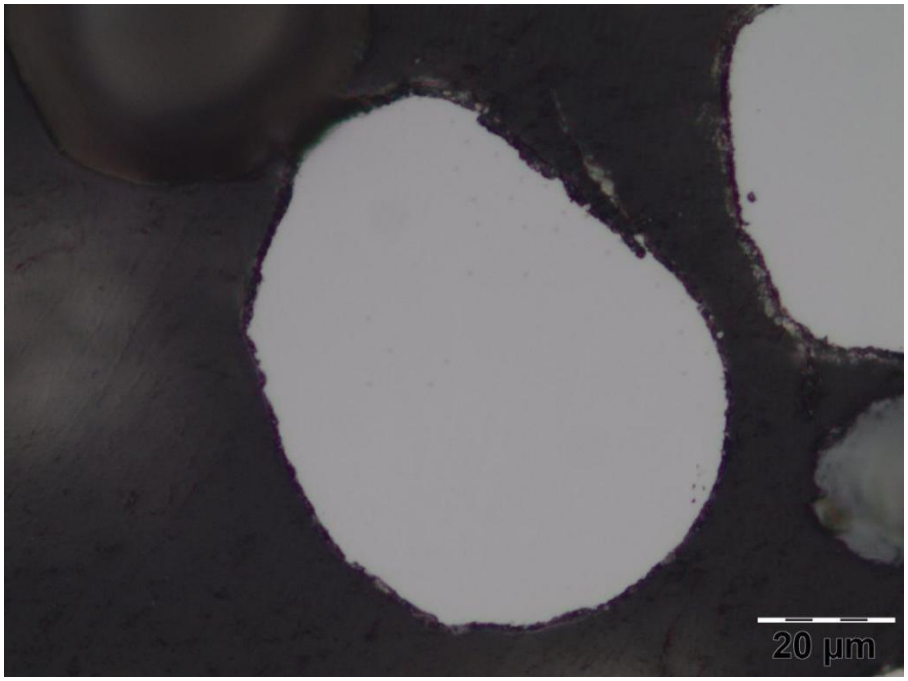

Figure B.8. Photomicrograph showing particle t30p5 in the as-polished condition

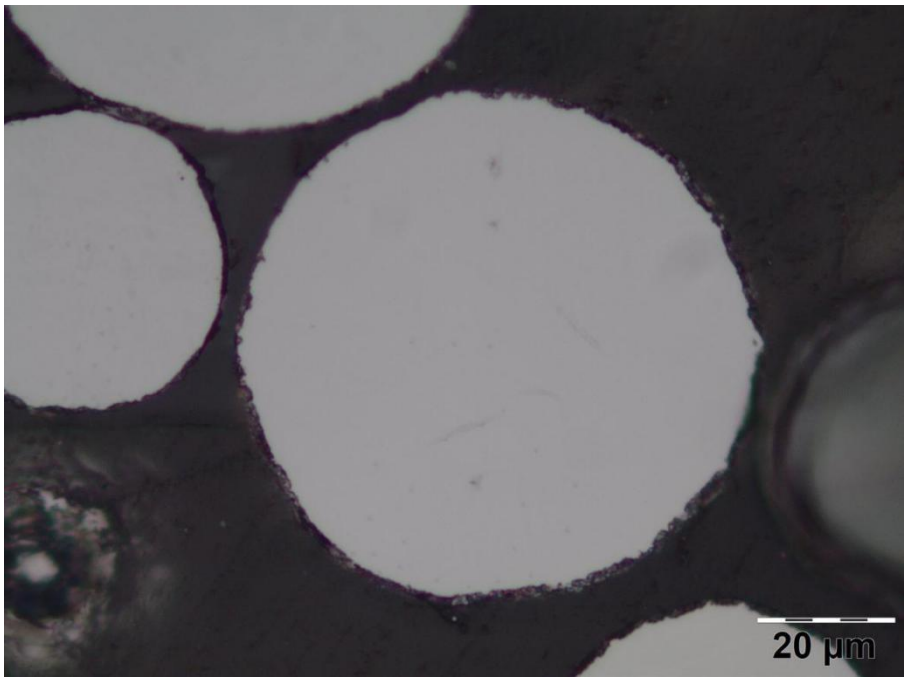

Figure B.9. Photomicrograph showing particle t30p6 in the as-polished condition

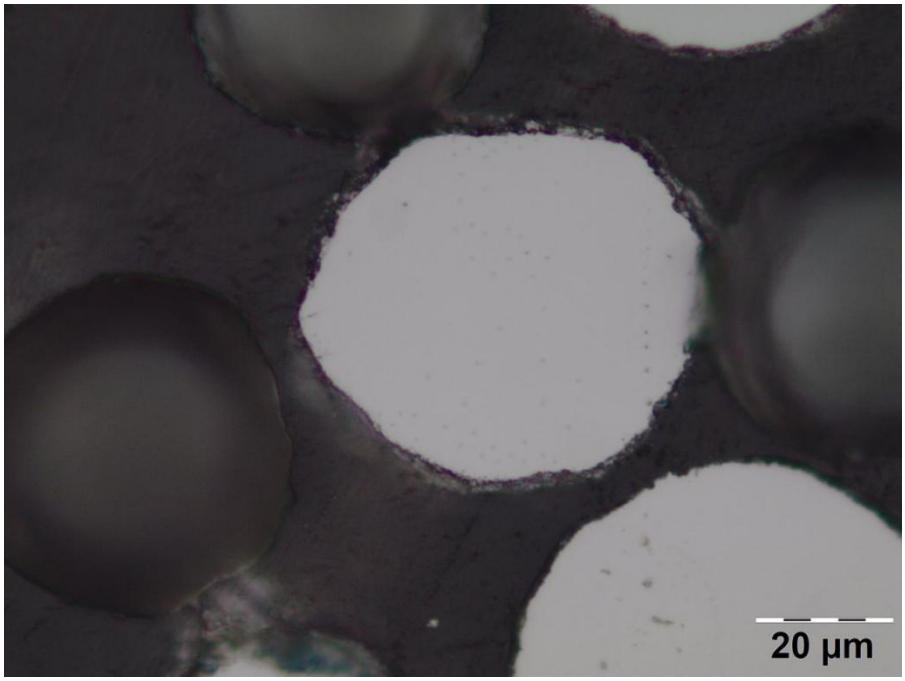

Figure B.10. Photomicrograph showing particle t30p12 in the as-polished condition

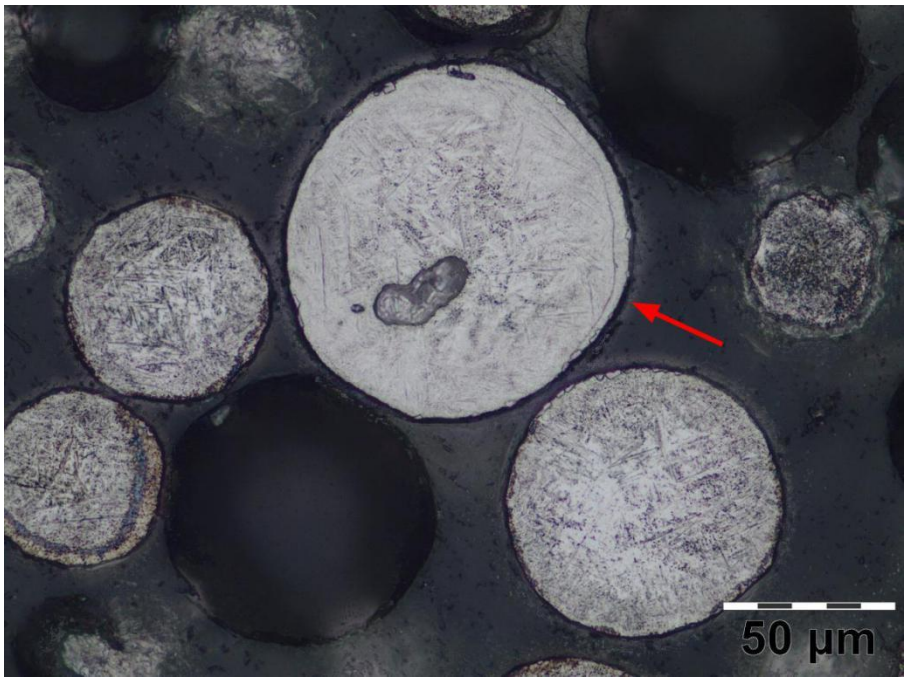

Figure B.11. Photomicrograph showing particle t30p10, indicated by the arrow, etched with Kroll's and ABF

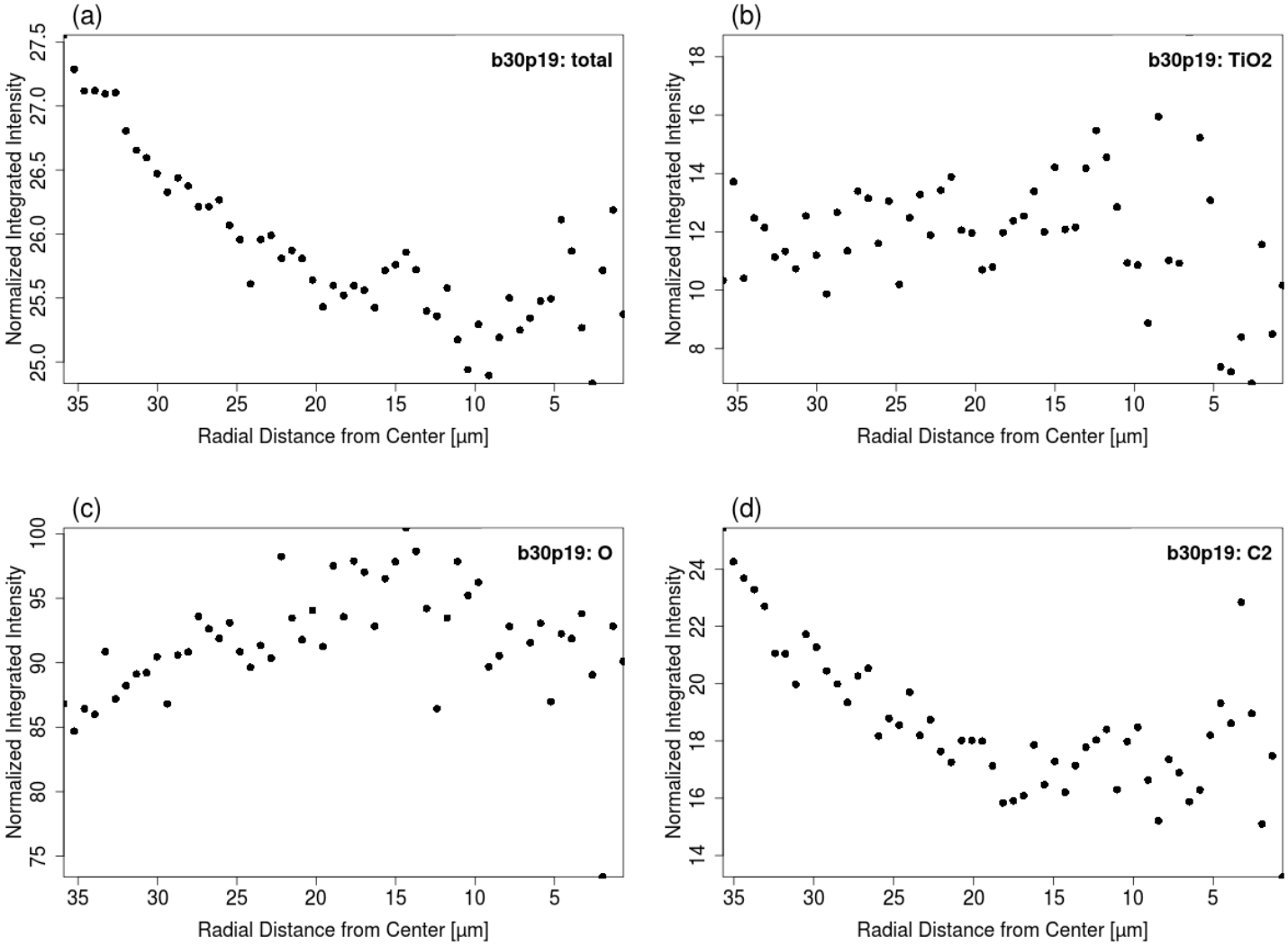

Figure B.12. ToF-SIMS radial integration plots for particle b30p19 showing the negative ion channel signal intensity for specific elements: (a) total ion spectrum, (b) TiO_2^- ion spectrum, (c) O^- ion spectrum, and (d) C_2^- ion spectrum

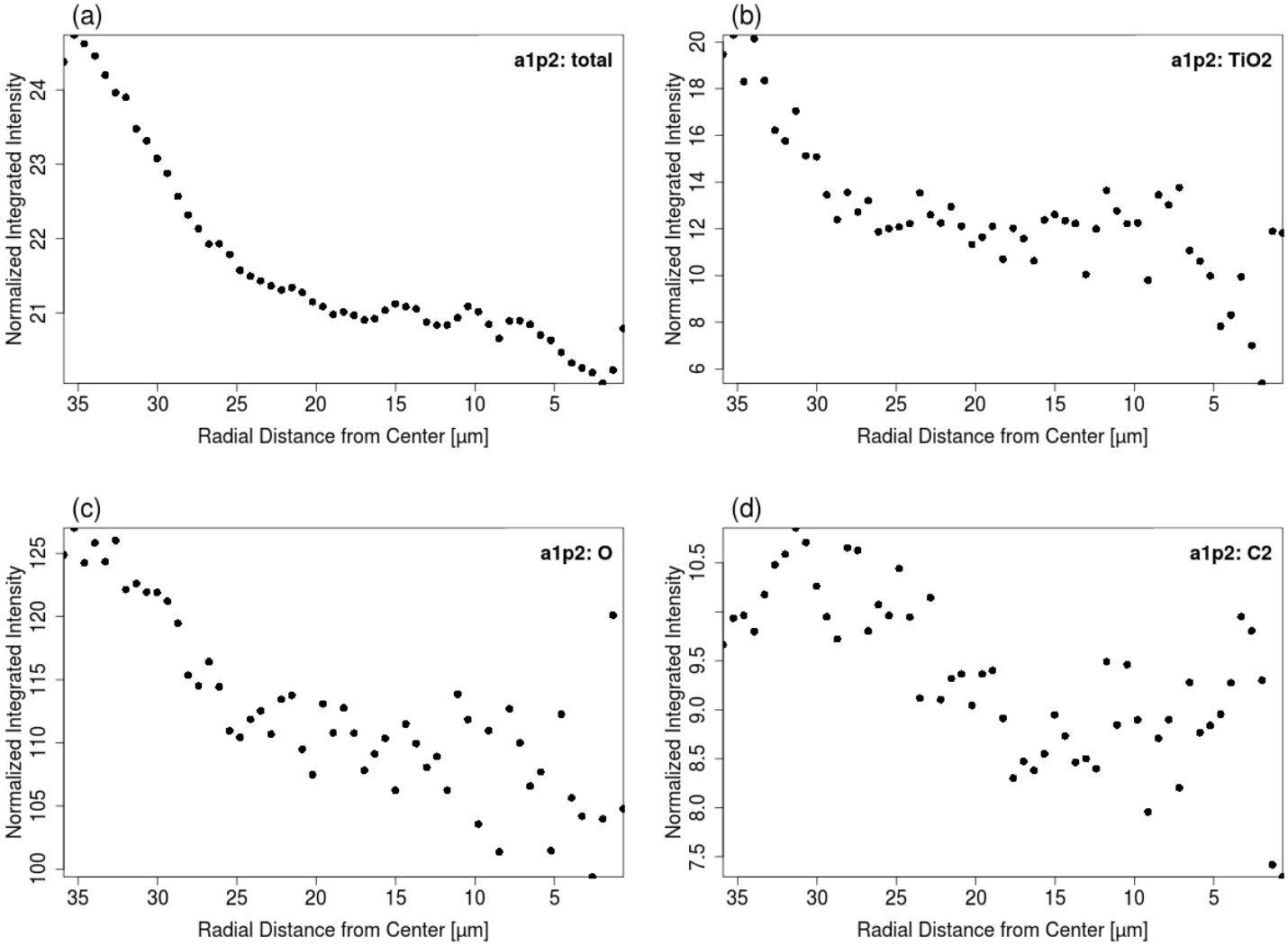

Figure B.13. ToF-SIMS radial integration plots for particle a1p2 showing select elements: (a) total ion spectrum, (b) TiO_2^- ion spectrum, (c) O^- ion spectrum, and (d) C_2^- ion spectrum

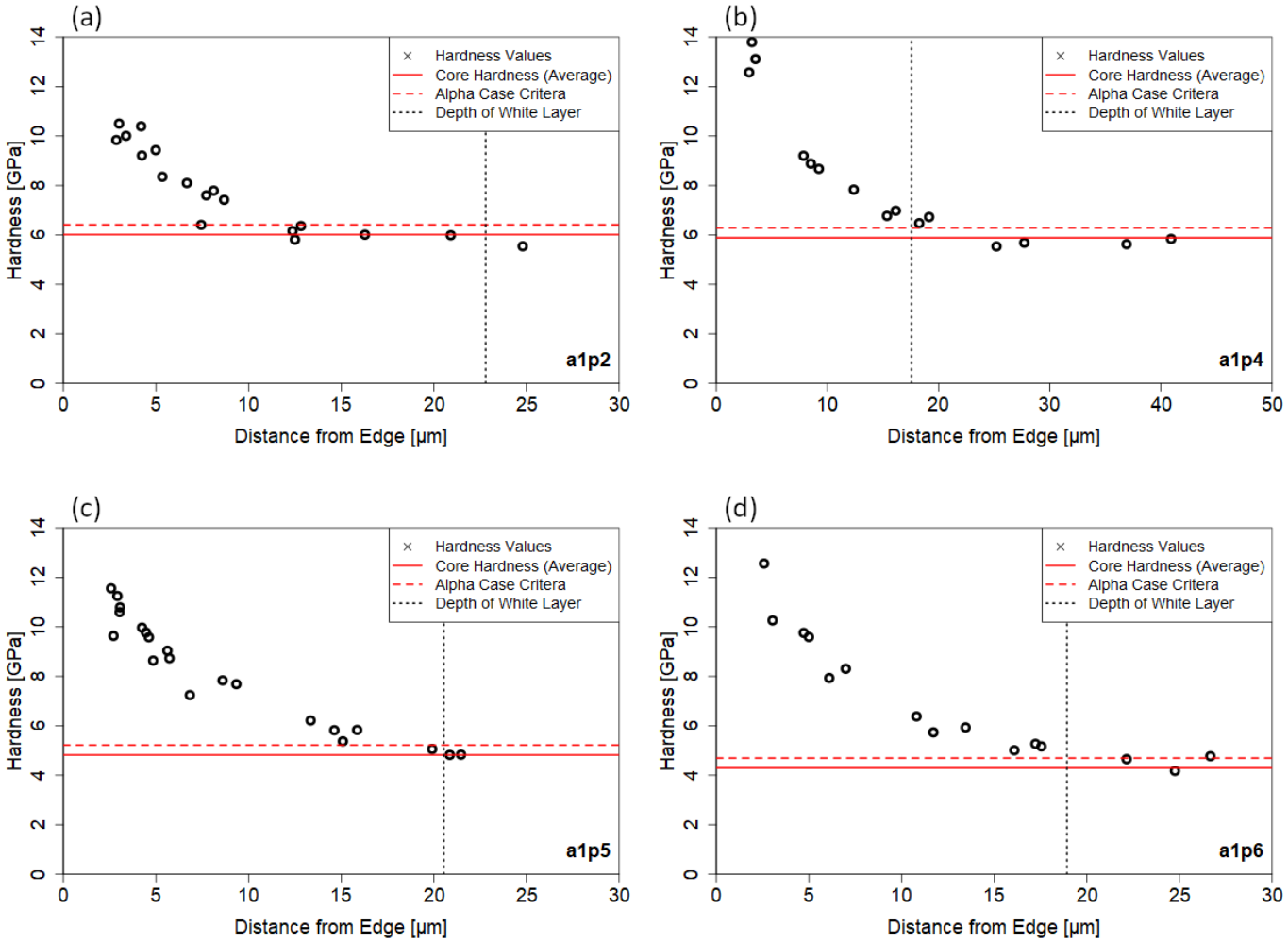

Figure B.14. Hardness depth profiles for particles (a) a1p2, (b) a1p4, (c) a1p5, and (d) a1p6. The solid red line indicates the core hardness (average of 5 readings); the dashed red line indicates a 0.4 GPa difference from the core average, indicating the defined alpha-case criteria; the dotted black line indicates the depth of the white layer as measured optically in the etched condition

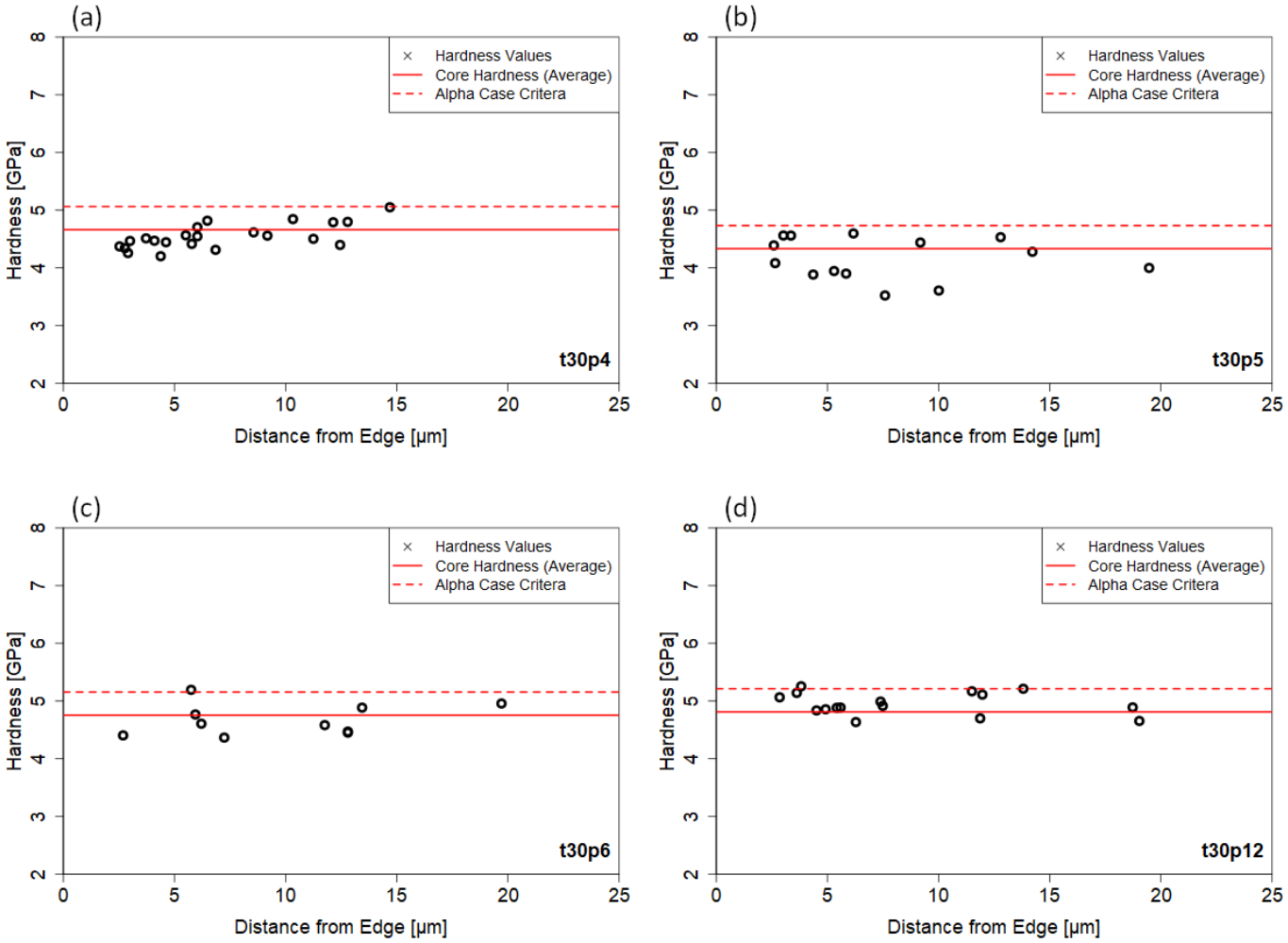

Figure B.15. Hardness depth profiles for particles (a) t30p4, (b) t30p5, (c) t30p6, and (d) t30p12 .The solid red line indicates the core hardness (average of 5 readings); the dashed red line indicates a 0.4 GPa difference from the core average, indicating the defined alpha-case criteria

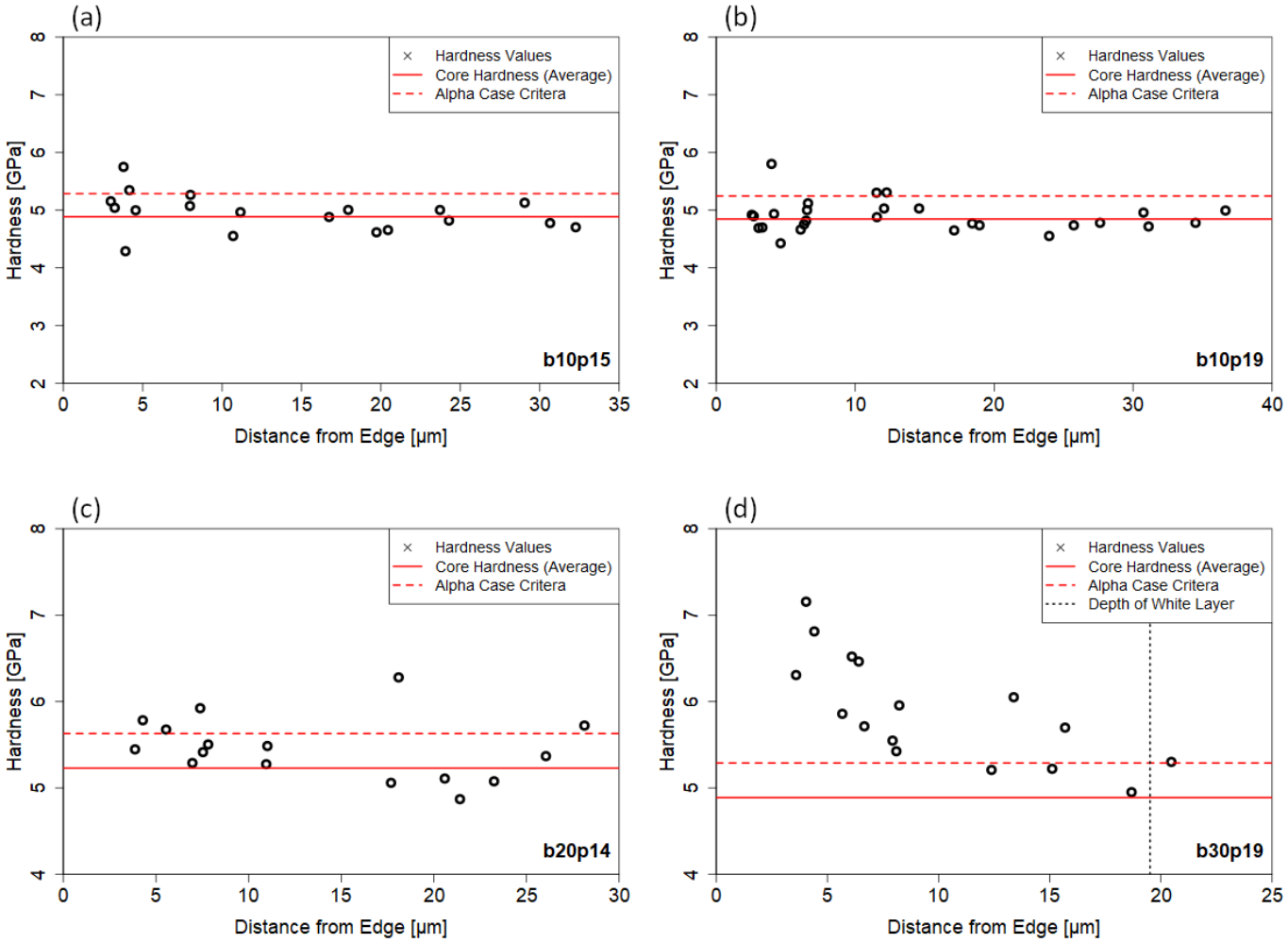

Figure B.16. Hardness depth profiles for particles (a) b10p15, (b) b10p19, (c) b20p14, and (d) b30p19. The solid red line indicates the core hardness (average of 5 readings); the dashed red line indicates a 0.4 GPa difference from the core average, indicating the defined alpha-case criteria; the dotted black line indicates the depth of the white layer as measured optically in the etched condition

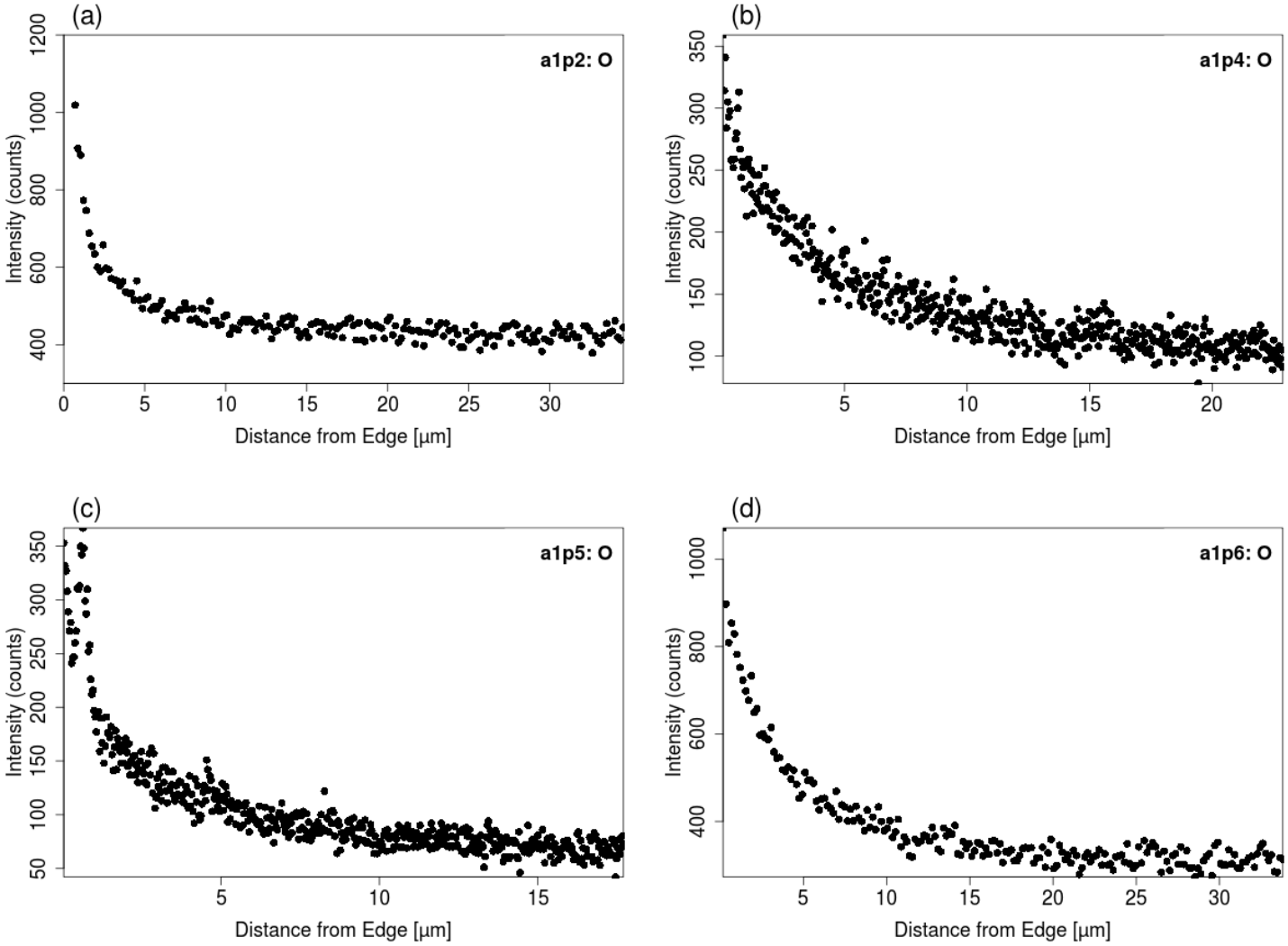

Figure B.17. EDS line scans showing oxygen signal intensity near the edge of particles (a) a1p2, (b) a1p4, (c) a1p5, and (d) a1p6

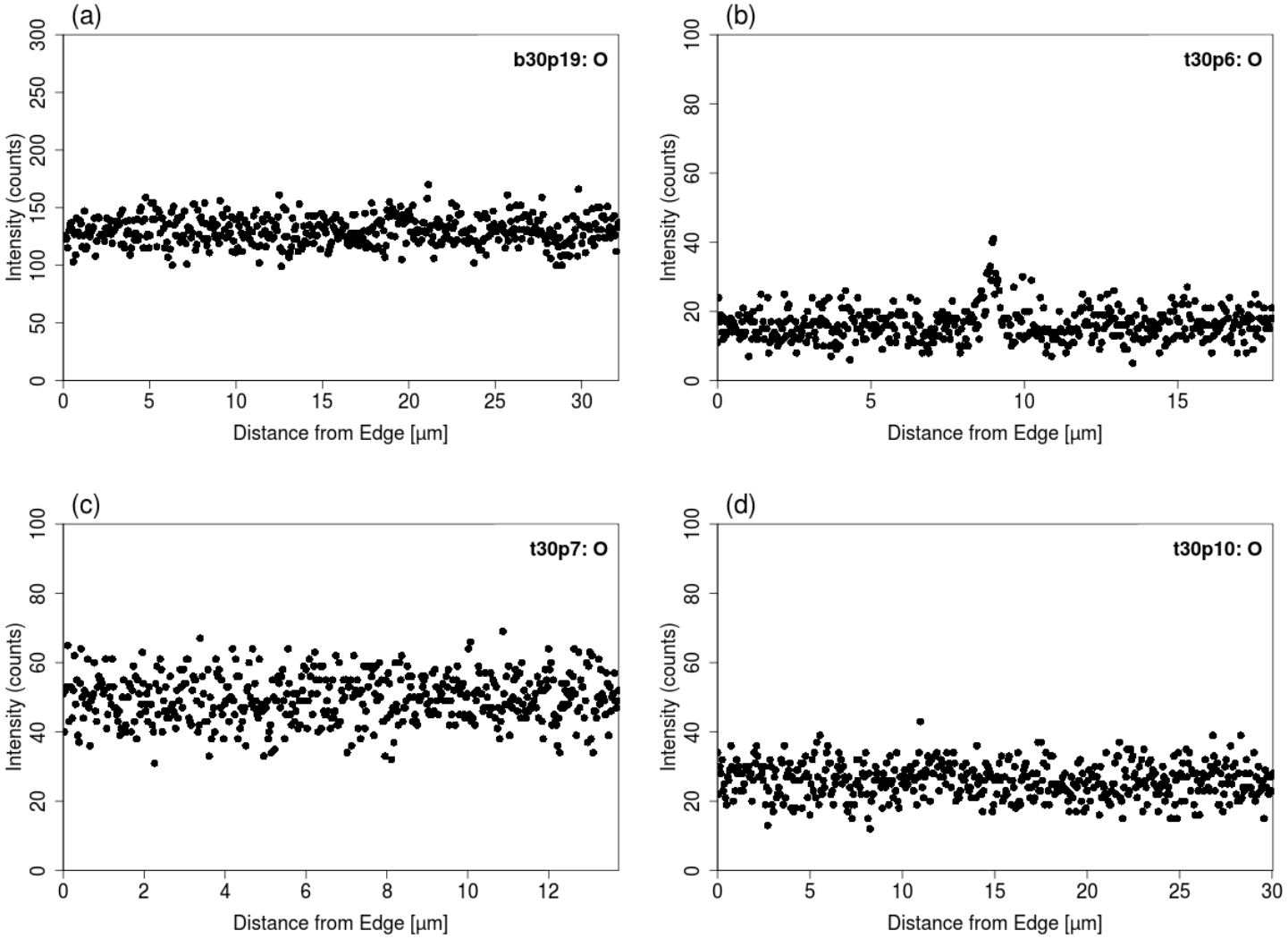

Figure B.18. EDS line scans showing oxygen signal intensity near the edge of particles (a) b30p19, (b) t30p6, (c) t30p7, and (d) t30p10

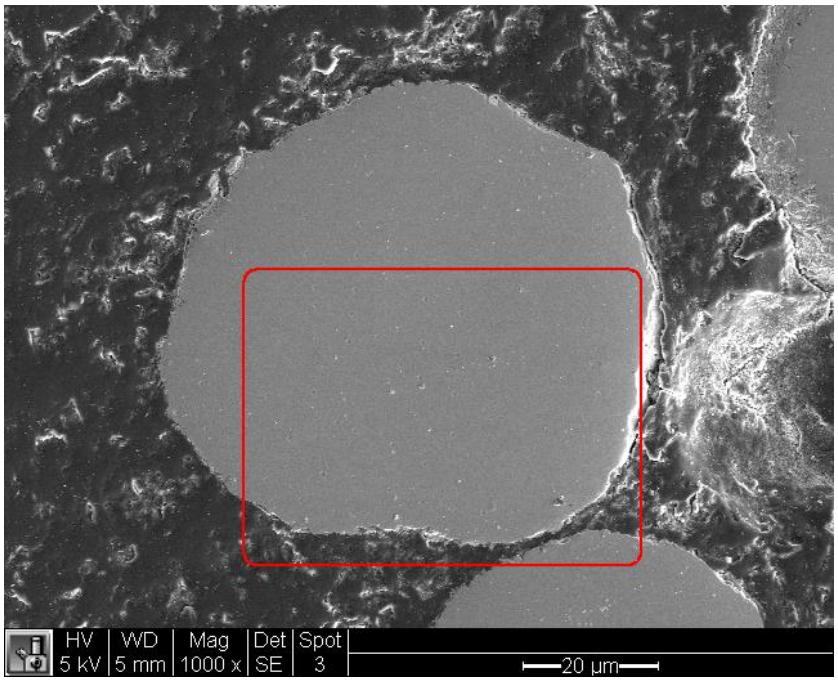

Figure B.19. SEM micrographs showing particle b30p9. The indicated area is shown at higher magnification in Figure B.20

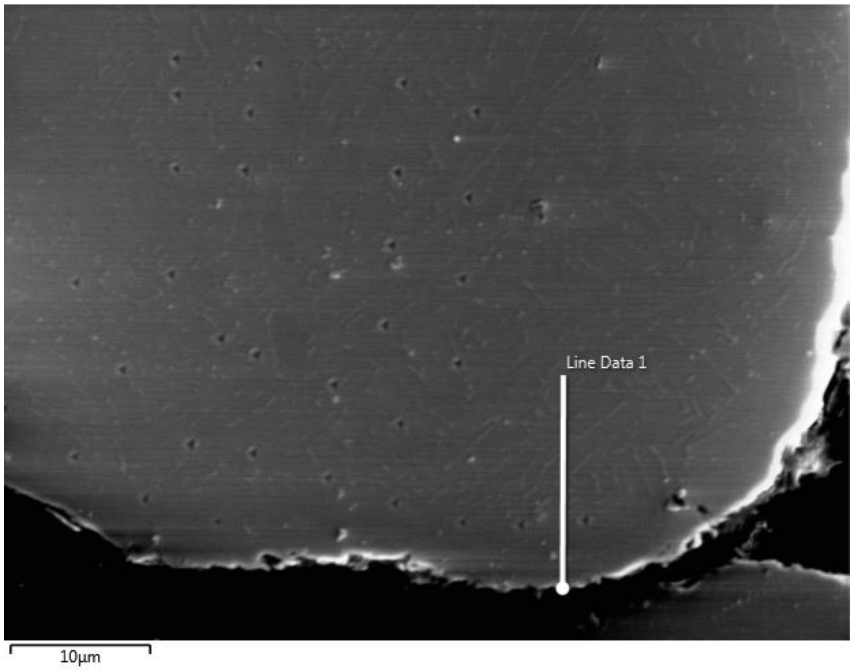

Figure B.20. SEM micrographs showing particle b30p9, with the location of the EDS linescan indicated. Indents from nanoindentation hardness testing are visible.

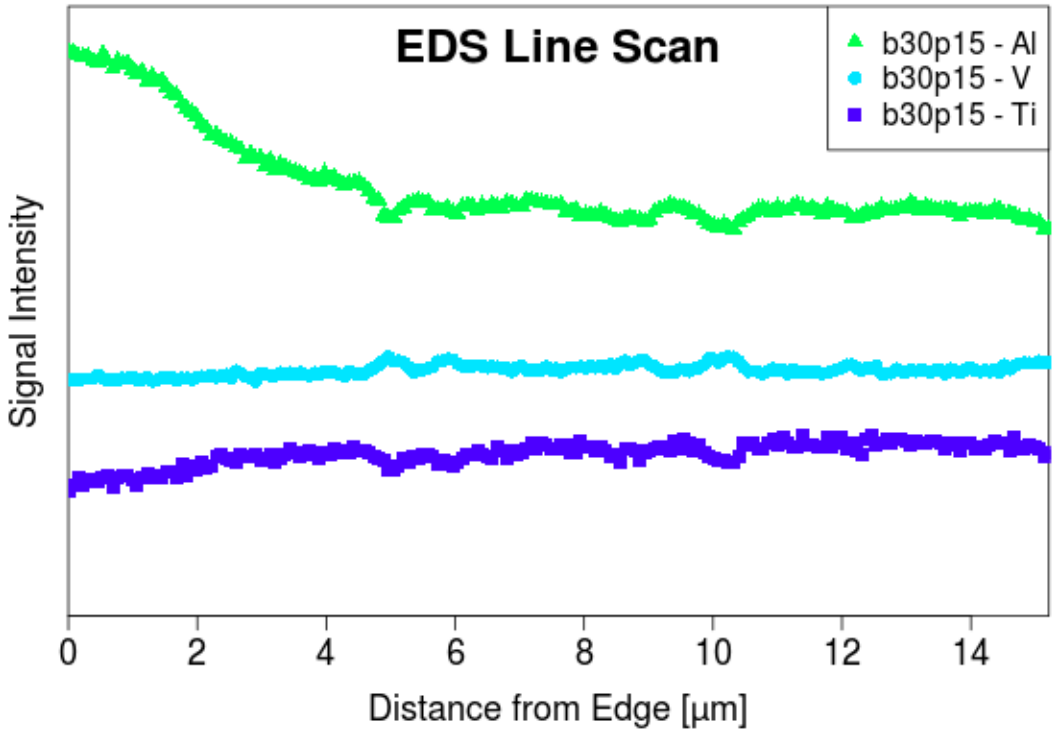

Figure B.21. Results of the EDS linescan on particle b30p9, showing an increase in Al signal near the edge of the particle.

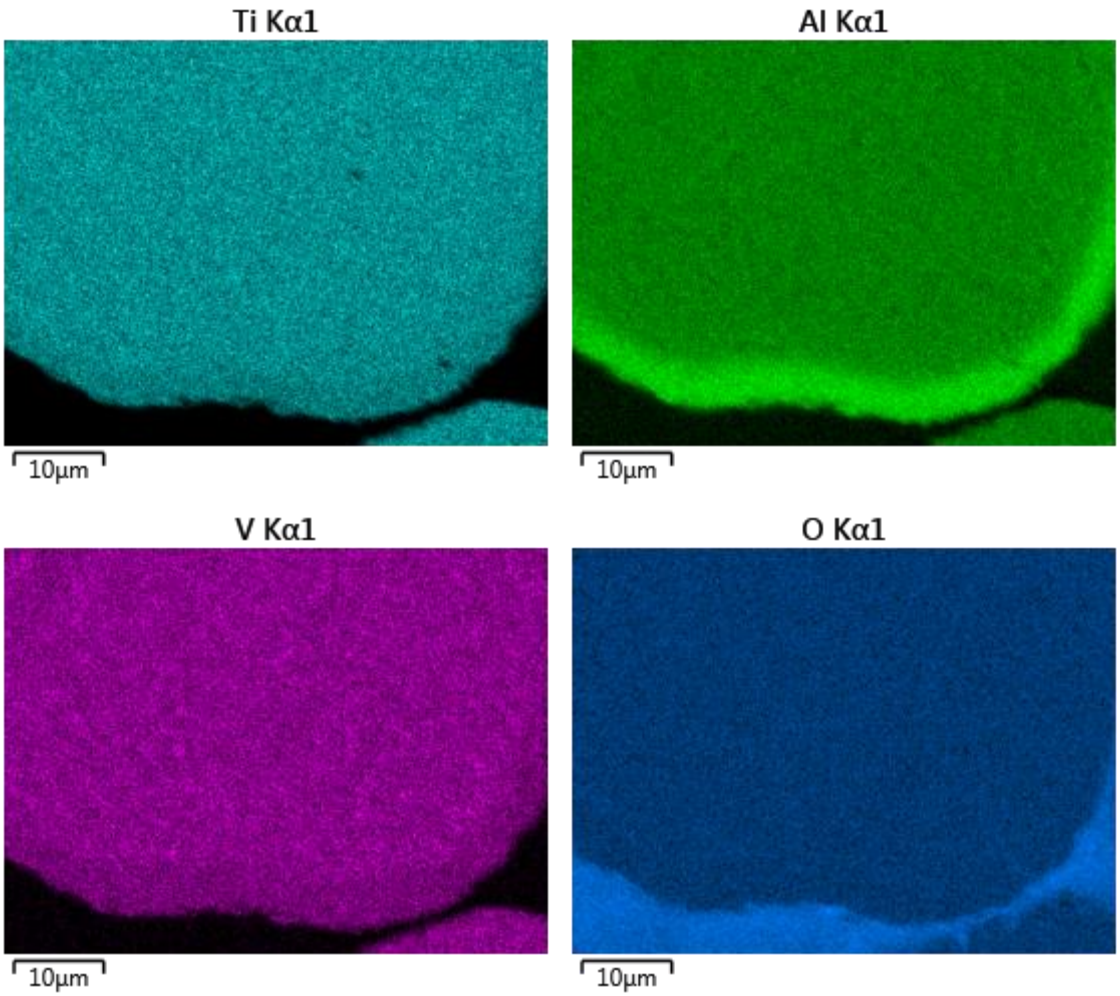

Figure B.22. EDS maps of the region of particle b30p9 shown in Figure B.20 showing the relative distribution of select elements. Brighter regions correspond to higher signal intensity.

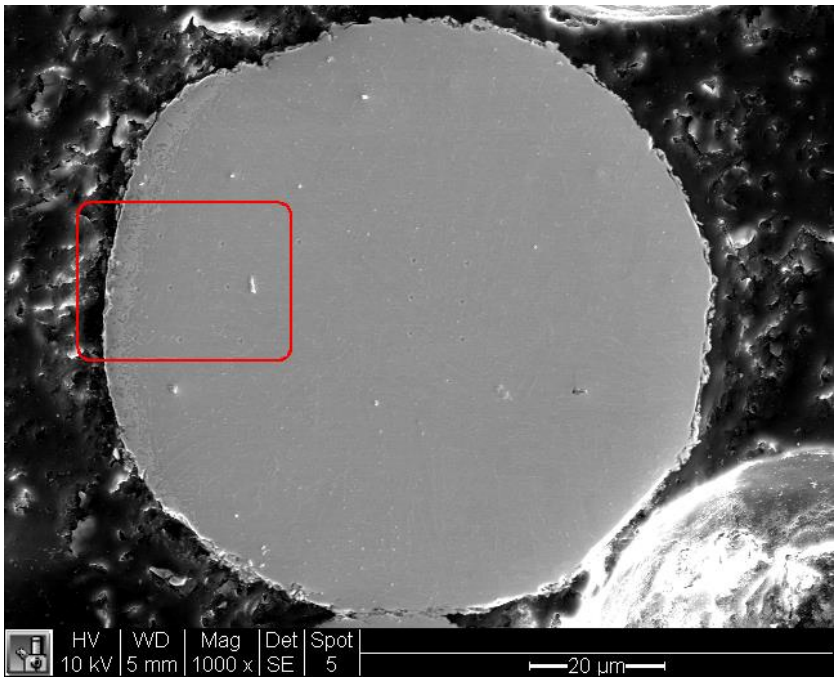

Figure B.23. SEM micrographs showing particle b30p15. The indicated area is shown at higher magnification in Figure B.24

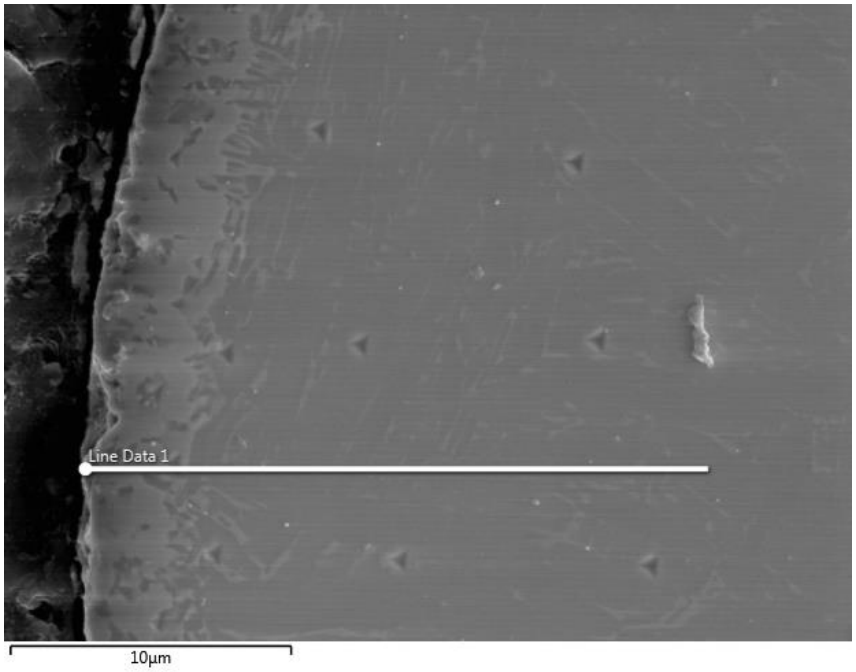

Figure B.24. SEM micrographs showing particle b30p15, with the location of the EDS linescan indicated. Indents from nanoindentation hardness testing are visible.

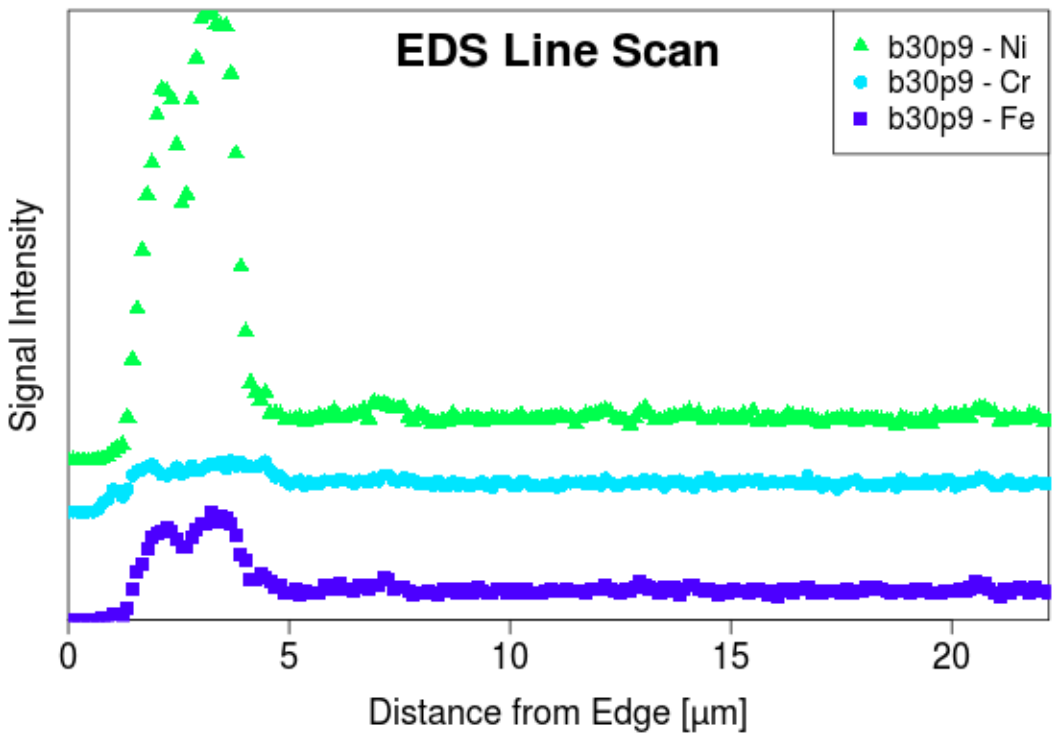

Figure B.25. Results of the EDS linescan on particle b30p15, showing an increase in Ni, Cr, and Fe signals near the edge of the particle.

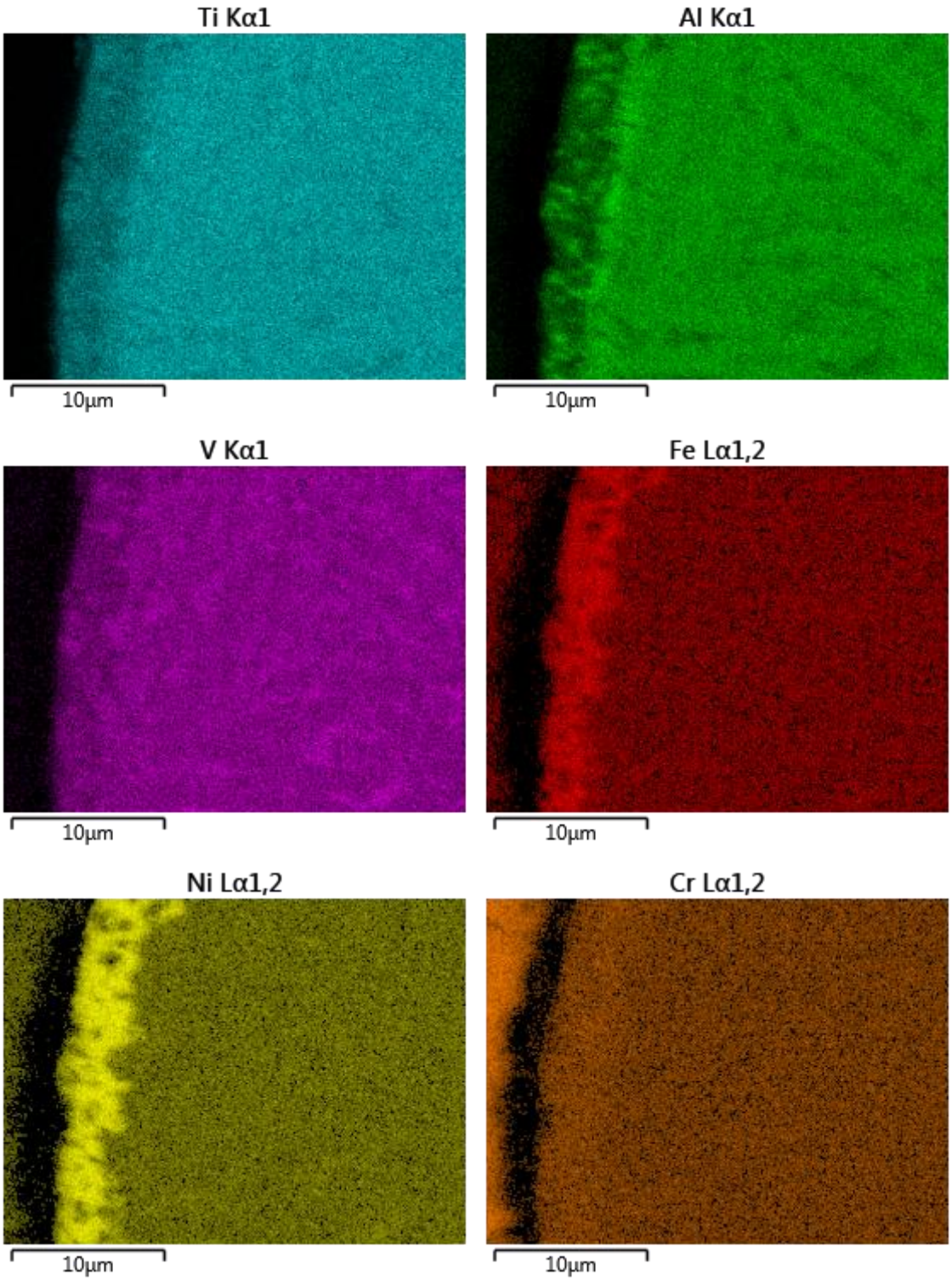

Figure B.26. EDS maps of the region of particle b30p15 shown in Figure B.24 showing the relative distribution of select elements. Brighter regions correspond to higher signal intensity